FRACTURE DETECTION AND WATER SWEEP CHARACTERIZATION USING SINGLE –WELL IMAGING, VERTICAL SEISMIC PROFILING AND CROSS-DIPOLE METHODS IN TIGHT AND SUPER-K ZONES, HARADH II, SAUDI ARABIA

A Thesis

by

HUSSAIN ABDULHADI A. ALJESHI

Submitted to the Office of Graduate Studies of
Texas A&M University
in partial fulfillment of the requirements for the degree of

MASTER OF SCIENCE

May 2012

Major Subject: Petroleum Engineering

Fracture Detection and Water Sweep Characterization

Using Single-Well Imaging, Vertical Seismic Profiling and Cross-Dipole

Methods in Tight and Super-K Zones, Haradh II, Saudi Arabia

FRACTURE DETECTION AND WATER SWEEP CHARACTERIZATION USING SINGLE –WELL IMAGING, VERTICAL SEISMIC PROFILING AND CROSS-DIPOLE METHODS IN TIGHT AND SUPER-K ZONES, HARADH II, SAUDI ARABIA

A Thesis

by

HUSSAIN ABDULHADI A. ALJESHI

Submitted to the Office of Graduate Studies of
Texas A&M University
in partial fulfillment of the requirements for the degree of

MASTER OF SCIENCE

Approved by:

Chair of Committee,	David S. Schechter
Committee Members,	Walter B. Ayers
	Richard L. Gibson
Head of Department,	Stephen A. Holditch

May 2012

Major Subject: Petroleum Engineering

ABSTRACT

Fracture Detection and Water Sweep Characterization Using Single-Well Imaging, Vertical Seismic Profiling and Cross-Dipole Methods in Tight and Super-K Zones, Haradh II, Saudi Arabia. (May 2012)

Hussain Abdulhadi A. Aljeshi, B.S., King Fahd University of Petroleum and Minerals

Chair of Advisory Committee: Dr. David S. Schechter

This work was conducted to help understand a premature and irregular water breakthrough which resulted from a waterflooding project in the increment II region of Haradh oilfield in Saudi Arabia using different geophysical methods. Oil wells cannot sustain the targeted oil production rates and they die much sooner than expected when water enters the wells. The study attempted to identify fracture systems and their role in the irregular water sweep.

Single-well acoustic migration imaging (SWI), walkaround vertical seismic profiling (VSP) and cross-dipole shear wave measurements were used to detect anisotropy caused by fractures near and far from the borehole. The results from all the different methods were analyzed to understand the possible causes of water fingering in the field and determine the reasons for discrepancies and similarities of results of the different methods. The study was done in wells located in the area of the irregular water encroachment in Haradh II oilfield. Waterflooding was performed, where water was

injected in the water injector wells drilled at the flanks of Harahd II toward the oil producer wells. Unexpected water coning was noticed in the west flank of the field.

While cross-dipole and SWI measurements of a small-scale clearly identify a fracture oriented N60E in the upper tight zone of the reservoir, the VSP measurements of a large-scale showed a dominating fracture system to the NS direction in the upper high-permeability zone of the same reservoir. These results are consistent with the directions of the three main fracture sets in the field at N130E, N80E and N20E, and the direction of the maximum horizontal stress in the field varies between N50E and N90E.

Results suggested that the fracture which is detected by cross-dipole at 2 to 4 ft from the borehole is the same fracture detected by SWI 65 ft away from the borehole. This fracture was described using the SWI as being 110 ft from top to bottom, having an orientation of N60E and having an angle of dip of 12° relative to the vertical borehole axis. The detected fracture is located in the tight zone of the reservoir makes a path for water to enter the well from that zone. On the other hand, the fractures detected by the large-scale VSP measurements in the NS direction are responsible for the high-permeability in the upper zone of the reservoir.

DEDICATION

I dedicate this thesis to my parents who are my first teachers after Allah. I also dedicate this work to my loving wife and to every member of my wonderful family. I must also be thankful for everyone who trusted me and supported me to reach my goals. Finally, I dedicate this work to my unforgettable grandmother, may Allah rest her soul in peace.

ACKNOWLEDGEMENTS

I would like to thank all of those people who helped me make this work possible.

First, I would like to thank my advisor, Dr. David S. Schechter, and my committee members, Dr. Walter B. Ayers and Richard L. Gibson, for all their guidance, help, and support throughout the courses and the research work.

I must thank my employer and sponsor company Saudi Aramco and its management for trusting and funding me and giving me this opportunity to learn, expand my knowledge and sharpen my skills. Appreciation is extended to my supervisor Mr. Rami Bin Nasser and Mr. Hussain Alali for their help.

I am also thankful for Baker Hughes Inc. for allowing me to use its facilities to conduct my research. Acknowledgement goes to Mr. Doug Patterson and his colleague Ms. Chun Lan for the time and effort they spent with me.

I would like also to recognize my great friends Zuhair Al Yousef and Ali Alali for their support as well as all my Aggies friends.

Finally, I will always be proud of being a member in the great entity Texas A&M University and thanks to my Aggie friends and colleagues and the department faculty

and staff for making my time in the state a pleasing and remarkable experience for the rest of my life.

TABLE OF CONTENTS

Page

CHAPTER Page

CHAPTER Page

LIST OF FIGURES

Page

Page

Page

Page

LIST OF TABLES

Page

CHAPTER I

INTRODUCTION AND FIELD REVIEW

1.1 Field Location and Dimensions

Haradh field forms the southern part of the supergiant Ghawar field. Because of that, Haradh has not been discussed in the literature as a standalone field, but included in Ghawar field reviews and discussion. I followed the same concept in this field review.

Ghawar field is located in the in the Eastern Province of Saudi Arabia about 80 km (50 mi) onshore from the Arabian Gulf, in Khobar County. It is about 100 km southwest of Dhahran where Saudi Aramco's headquarters is located **(Fig. 1)**.

This thesis follows the style of *SPE International.*

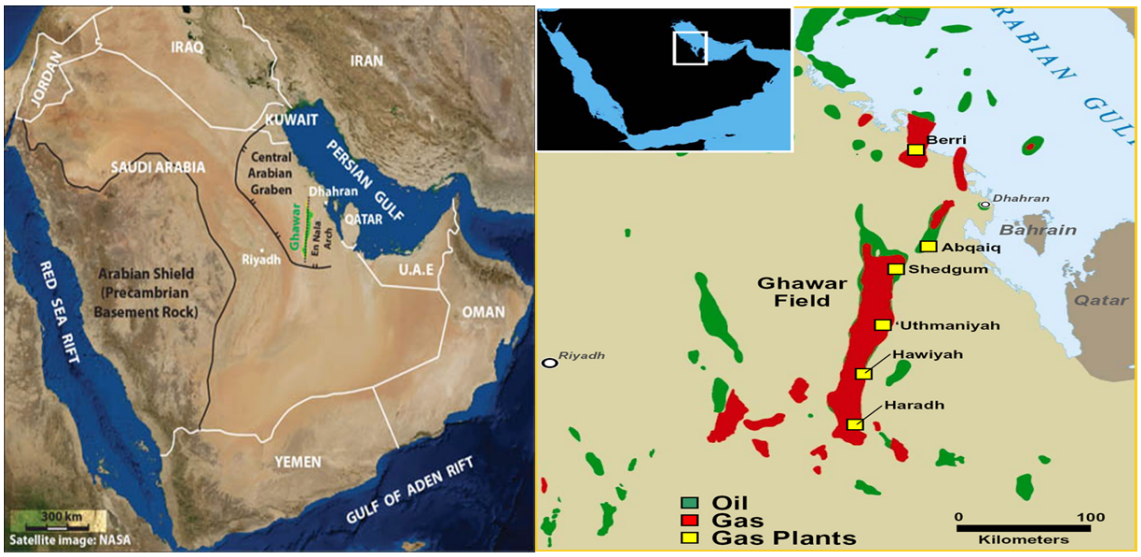

Fig. 1—Location of Ghawar field (Afifi, 2005; Sorkhabi, 2010)

Ghawar field is about 174 x 16 miles (280 x 26 kilometers), or a total area of around 2050 mi^2 (~ 1.3 million acres). The length of Ghawar field is about 70% of the distance from the north to the south of Louisiana (Afifi, 2005). In 1986 Alsharhan and Kendall estimated 2,800 km^2 of Ghawar is a productive area **(Fig. 2)** (Sorkhabi, 2010).

Fig. 2—Comparing Ghawar field to Louisiana (Afifi, 2005)

1.2 Mapping the Major Anticline

Ghawar field sits on an anticline structure called the En Nala ("the Slippers") anticline which is located is within the Central Arabian graben. This structure was first observed in 1940 by Ernie Berg, who was a geologist in of Standard Oil of California (Socal). While the company was drilling the Abqaiq prospect, Berg was mapping a dry riverbed in the Harahd area called Wadi Sabha. He noticed a sudden bend in the course of the Wadi Sabha from an east-west direction to the south. He assumed that a subsurface anticline trending north-south was the cause of the changing in path of the Wadi Sabha. Further work supported his assumption and the existence of the En Nala was accepted **(Fig. 3)** (Sorkhabi, 2010).

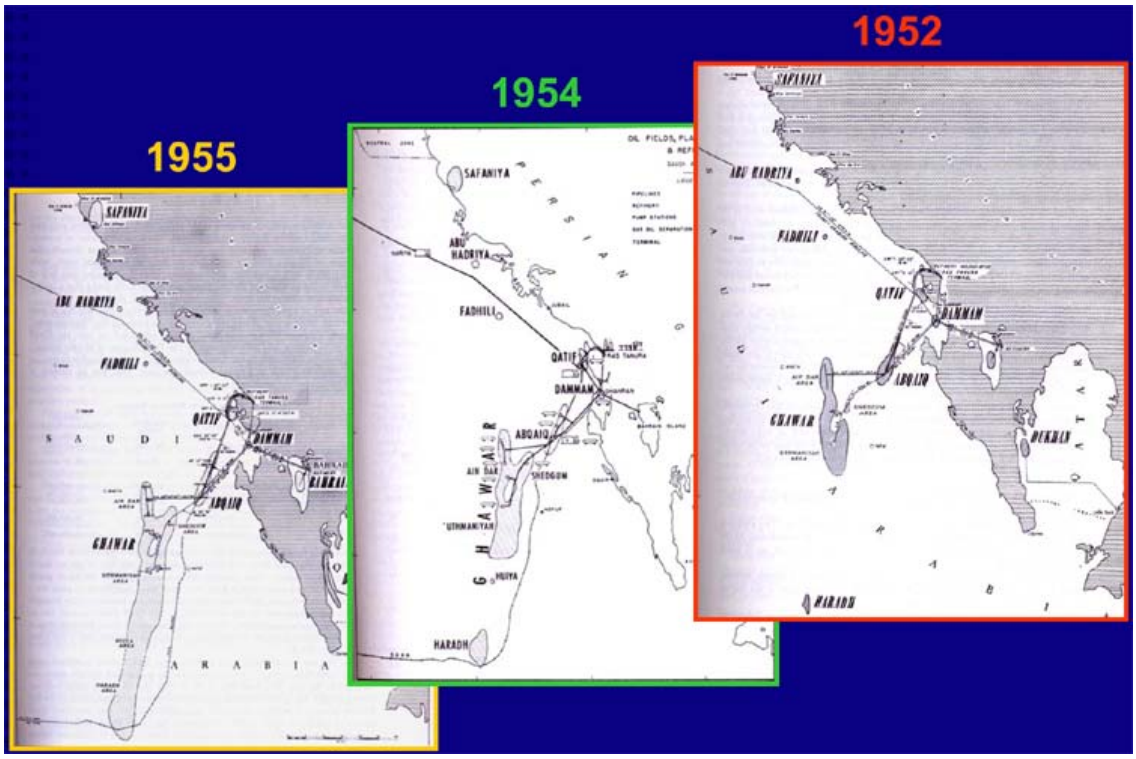

Fig. 3—Discoveries in Ghawar field (Afifi, 2005)

1.3 Geology of En Nala Anticline

Drilling and seismic images provided evidence that the Ghawar field sits on the En Nala anticline (trending N15° E) on a basement horst, which was created in the late Carboniferous-Permian extensional tectonics and block uplift caused by the continental rifting along the Arabia-Gondwana margin and opening of the Neo-Tethys Ocean. In the Late Cretaceous, this basement horst was reactivated as a compressional structure, which has continued in the Cenozoic as the Arabian plate collided with Asia. In the south, the En Nala structure forms a simple shallow, asymmetrical anticline with a steeper western

flank dipping is between 3° and 8°. The structure is more complex to the north **(Fig. 4)** (Sorkhabi, 2010).

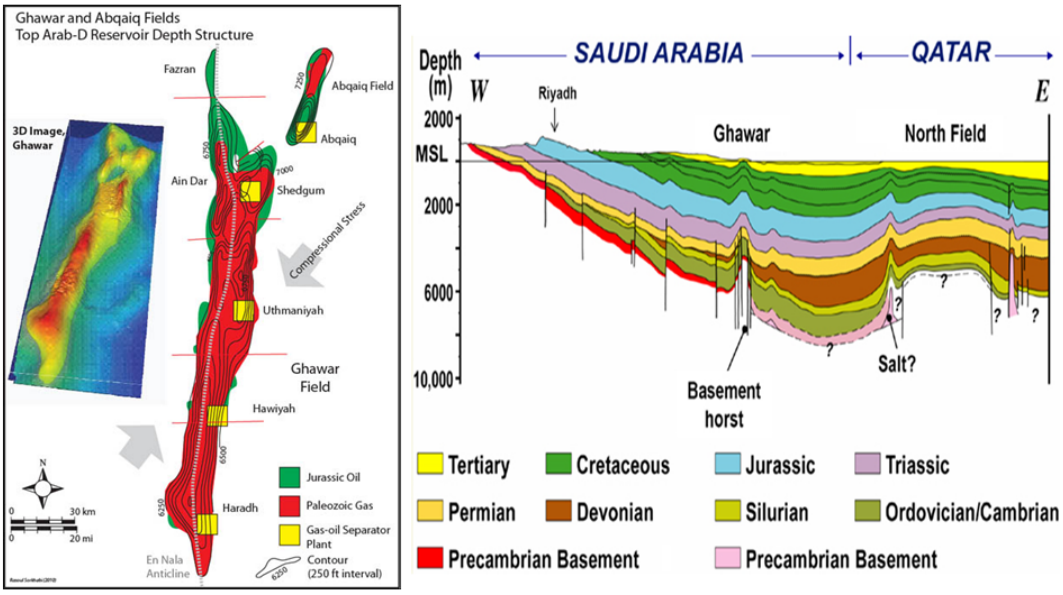

Fig. 4—Ghawar 3D image and location of En Nala anticline. The cross-sectional east-west map from the Arabian shield to the Persian Gulf shows the location of Ghawar field (Afifi, 2005; Sorkhabi, 2010)

1.4 The First Exploration Wells in the Ghawar

Based on the history of discovery, Ghawar was divided into six production areas from north to south:

1. Fazran
2. Ain Dar
3. Shedgum

4. Uthmaniyah
5. Haradh
6. Hawiyah

The first test well after the Second World War was drilled in 1948 at Ain Dar, and it hit oil. A second drill site was proposed at Haradh, about 185 km south of Ain Dar and also hit oil in 1949. Then Uthmaniyah No. 1 was drilled in 1951 followed by Shedgum No. 1 in 1952 and Hawiyah No. 1 in 1953. Oil was discovered in all the wells at depths between 2,000 m and 2,330 m (6,562 and 7,644 ft) along the same anticline from the same Upper Jurassic carbonate reservoir **(Table 1)**. All these discovery wells are still productive except Uthmaniyah No. 1.

In 1953, it was found that all these prospects were actually parts the world's largest single field that was named Ghawar, after the pasturage area the local Bedouins originally called Al Ghawar (Sorkhabi, 2010).

TABLE 1—GHAWAR'S FIRST 5 DISCOVERY WELLS

	Ain Dar #1	Haradh #1	Uthmaniyah #1	Shedgum #1	Hawiyah #1
Discovery	1948	1949	1951	1952	1953
Onstream	1951	1964	1956	1954	1966
Initial Rate barrels/day	15,600	6,400	11,300	12,400	4,800
Enhanced recovery	1999 water	1990 acid	1964 water	1968 acid	1977 acid
Production (million bl) to 2008	152	24	20	98	51
Production barrels/day in 2008	2,100	2,300	None	3,700	4,600

1.5 The Major Jurassic Reservoir

The Upper Jurassic Arab formation forms the major oil reservoir in the Middle East. In Ghawar, the Arab D reservoir extended from the lowermost zone of the Arab formation to the uppermost part of the Jubaila formation. It is a carbonate rock of Kimmeridgian age was deposited on the shelf of the Neo-Tethys Ocean. The Ghawar area lies about 5° south of the equator. The Arab formation is 186 m (610 ft) thick and Jubaila formation is 400 m (1312 ft) thick in Ghawar. The producing interval is between 50 and 100 m (164-328 ft). Arab D carbonates are also further divided into smaller units (Sorkhabi, 2010).

1.6 Arab D Units

The Arab D carbonate reservoir is divided into four zones, starting with Zone 1 on the top and ending with Zone 4 at the bottom. Zone 1 is a nonproductive zone of low

porosity and low permeability. Zone 2 is divided into Zone 2A and Zone 2B. Zone 2A is mostly skeletal oolitic limestone with scattered vugs. Zone 2B commonly includes dolomite and cladocoropsis, evidenced by a very high-permeability zones or what is called a super-permeability (super-k) phenomenon. Zones 3A and 3B have much poorer reservoir quality and permeabilities (Figs. 5 and 6) (Al-Anazi, 2007; Croft 2011; Pham et al., 2003).

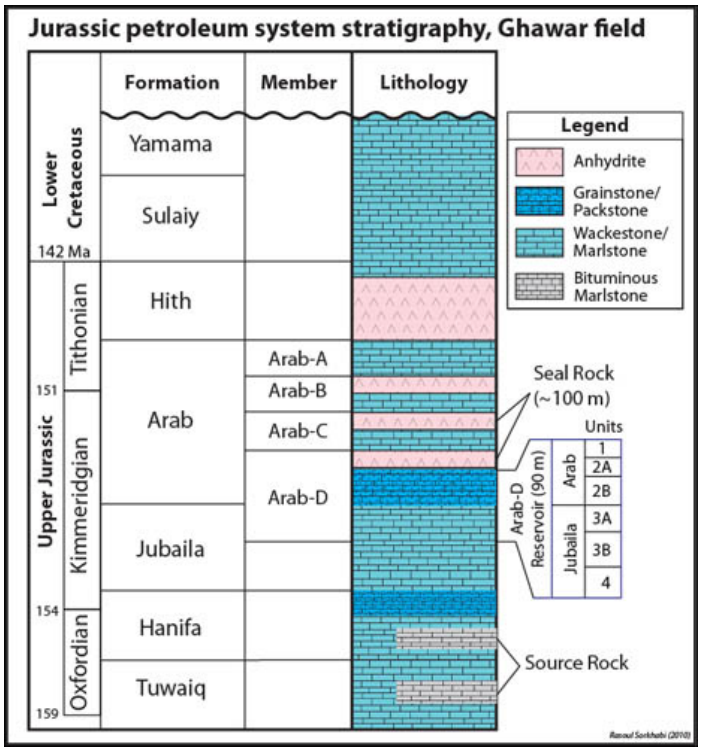

Fig. 5—The stratigraphic column of Ghawar field (Sorkhabi, 2010)

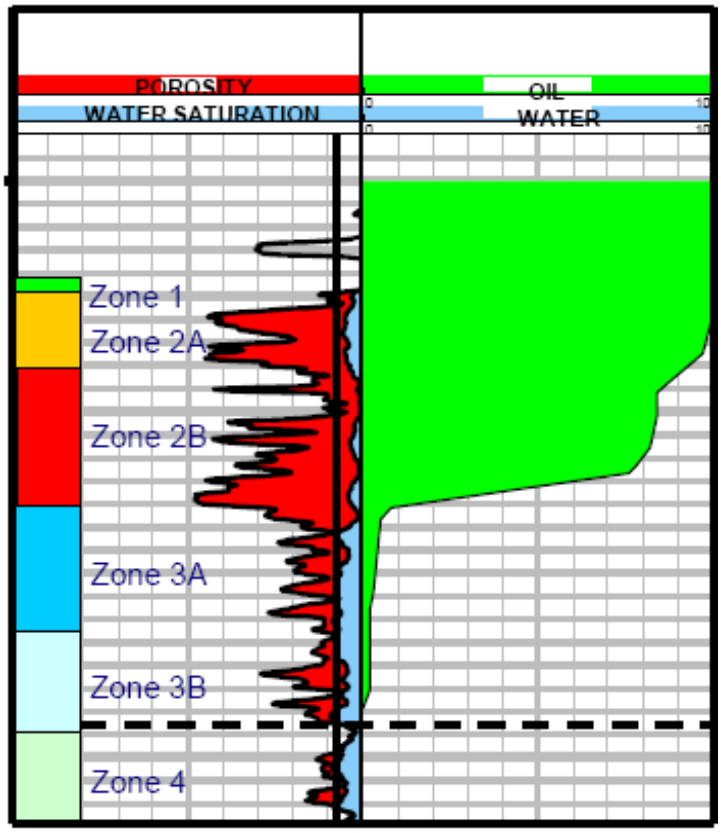

Fig. 6—Arab D reservoir is divided into different zones of different porosity and productivity (Pham et al., 2003)

1.7 Source Rock

The Arab D reservoir is sourced from the Tuwaiq Mountain formation below the Jurassic Hanifa formation. It is a marine shelf deposit of mud and lime with as much as 5% organic material. A good oil source rock, it is 1% to 7% organic rich. It is Callovian and Oxfordian in age and its thickness is more than 90 m (300 ft) in the basinal area between the Ghawar and Khurais fields. The seal is an evaporitic package of rocks including impermeable anhydrite (Al-Anazi, 2007; Croft 2011).

1.8 Haradh Field

Haradh is the southern part of the Ghawar field and is divided into 3 areas called Haradh increments I, II, and III. Increment I was produced in May 1996 followed by Increment II in April 2003 and Increment III in January 2006 (Al-Mubarak et al., 2007). The Harahd II is the focus of this study. Haradh II is approximately 30 km (19 miles) from east to west and and 20 km (20 miles) from north to south (Pham et al., 2003). The Haradh Arab D parameters are summarized in **Table 2**.

TABLE 2—HARADH AREA, ARAB D RESERVOIR PARAMETERS, SAUDI ARAMCO (1980) (Croft 2011)

Original OWC in Feet Subsea	6000 to 6620
Average Net Thickness (Feet)	140
Formation Volume Factor (RB/STB)	1.27
Initial Solution Gas-Oil Ratio (SCF/Bbl.)	470
Oil Gravity (Degrees API)	32
Oil Viscosity at Reservoir Conditions (centipoise)	0.89
Sulfur Content, by Weight	2.15 %
Average Porosity	14 %
Average Permeability (Millidarcies)	52
Water Saturation (Original)	11 %
Average Productivity Index (BOPD/PSI)	31

1.9 Waterflooding Project in Harahd

The initial average reservoir pressure in the Ghawar was more than 3200 psia at 6,100 ft subsea. In the north part of the field at Ain Dar field, the bubblepoint pressure is around 1,900 psia, and in the southern part at Haradh field it is around 1,700 psia. Although the Ghawar field was discovered in the early 1950's, the pressure maintenance project was not started until the middle of the 1960's when pressure depletion was noticed. Because of its huge volume, the original aquifer did not have the capability to provide the compulsory pressure support.

From 1966 until 1973, waterflooding was gravity-fed water sourced form a freshwater aquifer (5,000 ppm TDS) near the Al-Hasa Oasis. Pressured water injection started in 1973 and freshwater sourcing was replaced by Persian Gulf seawater (56,000 ppm TDS) (Voelker, 2004).

1.10 Fractures in Haradh

Haradh is a highly fracture area. In Haradh I, wells were drilled and completed as vertical wells. Especially at the west flank, wells produced high water content and had to be shut in. Also, well-completion penetrating fractures would began producing water almost immediately and soon die.

Lessons learned from Haradh I were considered during the Haradh II development. Simulation model results of Haradh II showed that vertical wells would not maintain the

desired production plateau for even 2 years. On the other hand, replacing the vertical wells with horizontal producers and water injectors might maintain the production for as long as 15 years (Simmons, 2005).

1.11 Fractures Sets

Fractures are basically the results of compliance or adaptation to in-situ stress. When the applied stress passes the breaking point of the rock, it breaks. The maximum stress direction of the reservoir does not have to be static through the history. Changing stress direction of the field through time causes the development of different fracture systems in the reservoir. Usually, water will move faster in the fractures that align in the maximum current stress direction because they are more conductive than others. During the characterization phase of Haradh, three main set of fractures were founded in Haradh Arab-D, at N130E, N80E and N20E. The direction of the fractures in the reservoir suggests that some rotation may have happened in different locations of the reservoir. Pham and et al. (2003) simulated these fractures as two sets. The first set included fractures in the N130E direction and the second set included fractures in the N80E and N20E. These fractures appear to be open fractures **(Fig. 7)** (Pham et al., 2003; Stenger et al., 2001).

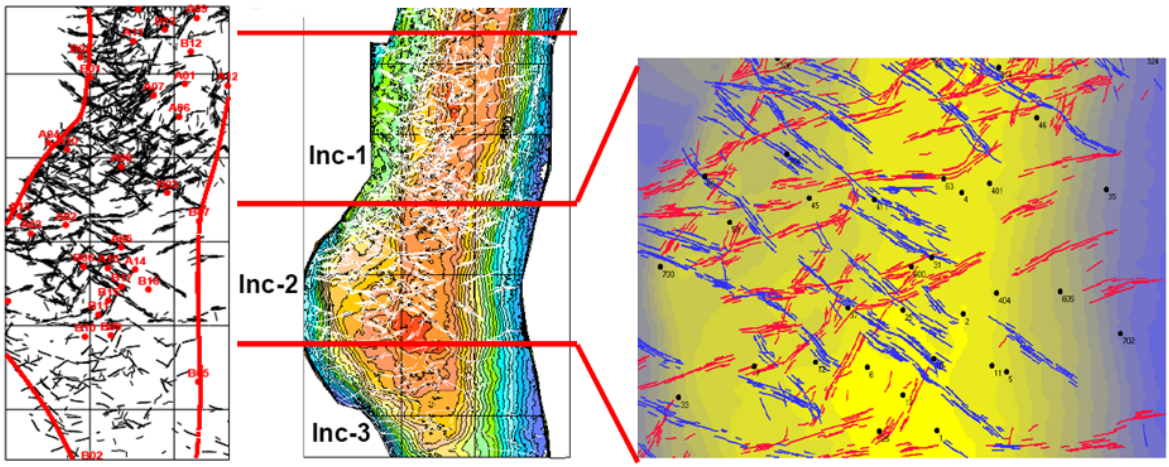

Fig. 7—Haradh field is a highly fractured field. The main three directions of fractures are divided into two sets in the reservoir modeling. In the fracture model, the Haradh field is divided into two sets. In the most-right plot, the red fractures are in N20E and N80E and the blue fractures are in the N130E (Pham et al., 2003; Stenger et al., 2002)

1.12 Water Fingering and Connected and Conductivity

Pham and et al. (2003) found that water fingering is more important with the connected and conductive fracture network. Because of that, wells intersecting the fracture network will water out and die prematurely. However, these open conduits of the fracture networks play a vital role in sustaining high oil production by providing the required pressure maintenance from the injectors.

1.13 Direction of Horizontal Producers

The horizontal wells were planned to be parallel to the main and high-conductivity fracture directions to keep water cut low for as long as possible during the well life. The most conductive fractures are those which are parallel to the maximum stress direction

(N50E). That places the producer well placement window between N70E and the EW direction. This result was approved during the drilling phase, and wells drilled outside this window had lost circulation during drilling and higher water cut when produced **(Fig. 8)**. Therefore, the development strategy was to place the first row of producers through both Zone 2A and Zone 2B to intersect the super-k bodies. The second row of producers was planned to be completed through the top of Zone 2A to delay the water encroachment (Pham et al., 2003; Stenger et al., 2001).

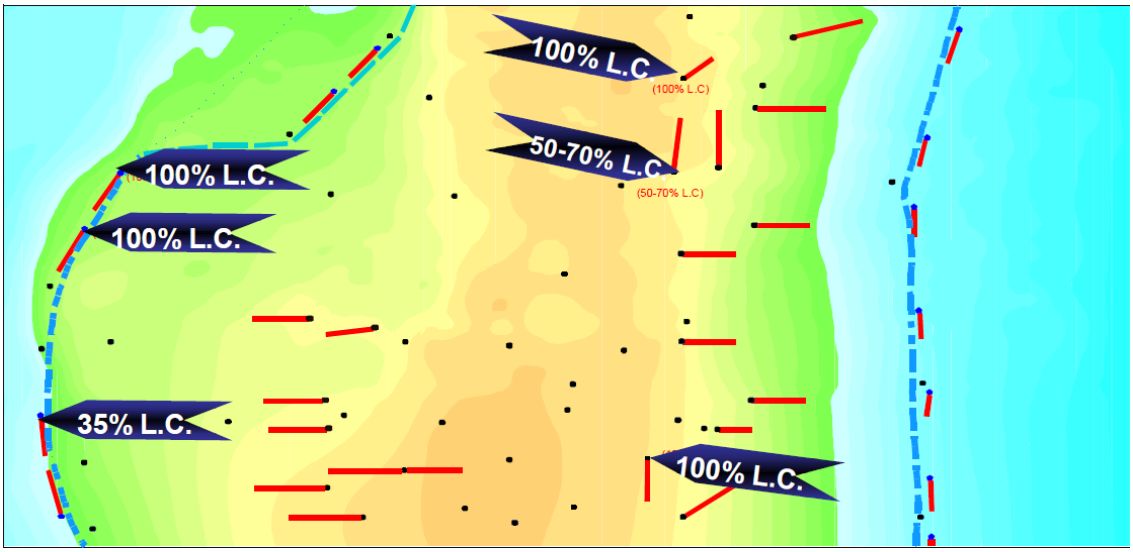

Fig. 8—Loss circulation map and trajectory of the horizontal producer and injector wells drilled in the Haradh II (Pham et al., 2003)

1.14 Direction of Horizontal Injectors

The horizontal water injector wells were planned to be placed parallel to the oil/water contact, mainly in the north-south direction, and to intersect the high-conductivity fracture network. Doing that provided higher pressure support for the field (Pham et al., 2003).

CHAPTER II

ACOUSTIC WAVE PROPAGATION PRINCIPLES

2.1 Waves Propagation

Formations are divided into two types. Formations with S-wave velocity faster than the borehole fluid (mud) velocity are called fast formations. Formations with S-wave velocity slower than the mud velocity are called slow formations. In a fast formation, when a monopole source is fired at the center of a borehole, a sound wave propagates in all the directions around the source as a spherical compressional wave. Once this wave contacts the borehole wall, it is divided into three different types of waves. One type of wave is reflected in what is called a trapped or guided mode. The other types are the refracted, the compressional wave (primary waves), and the refracted shear waves (secondary waves). Snell's law explains how these three different types of waves were generated and detected (Haldorsen et al., 2006). The principle is illustrated in **Fig. 9.**

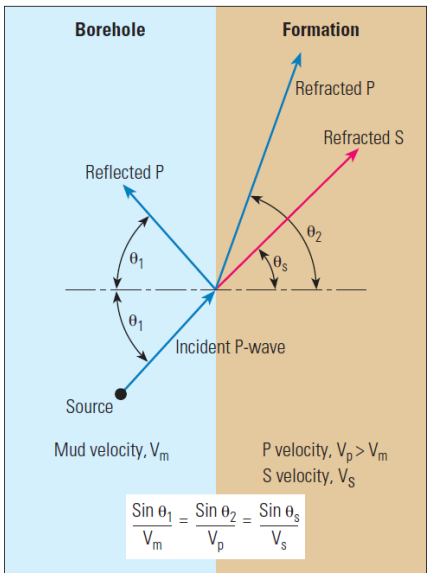

Fig. 9— Snell's law applied to a wave traveling from borehole filled with mud of velocity V_m into formation with compressional wave velocity V_p and shear wave velocity V_s. Head waves are created when the angle of refraction equals 90° (Haldorsen et al., 2006).

Snell's law states that when a wave travels between two media such that the velocity of medium 1 is less than the velocity of medium 2 ($V_1 < V_2$), the ratio of the sine of the angles of incidence and refraction is equivalent to the ratio of phase velocities in the two media:

$$\frac{\sin\theta_1}{\sin\theta_2} = \frac{V_1}{V_2} \quad \text{..... 1.2}$$

When the angle of incident (θ_1) reaches what is called the critical angle (θ_C), the refraction angle (θ_1) equals 90° and the ratio becomes:

$$\frac{\sin\theta_C}{1} = \frac{V_1}{V_2} \quad \text{.....1.3}$$

In this situation the refracted P-waves and S-waves travel parallel to the borehole, and head waves are generated inside the borehole. Head waves are compressional waves. That explains how the shear wave, which does not propagate in fluid, can be detected. The P head waves and the S head waves travel at the same velocities of formation P velocity and S velocity. Formation P and S velocities can be determined from P head waves and the S head wave velocities (Close et al., 2009). Wave propagation and head wave creation are shown in **Fig. 10.**

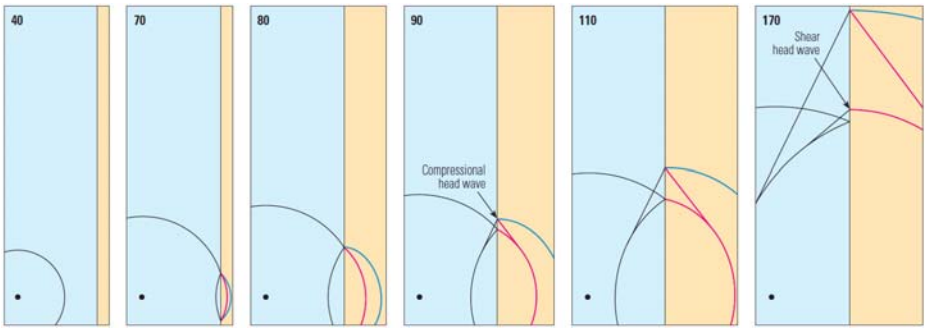

Fig. 10—Compressional head waves and shear head waves are created as time pass (from 40 to 170 μs) while the compressional wave created by the acoustic source in the mud travels into the formation (Haldorsen et al., 2006).

2.2 Acoustic Waves

Monopole and dipole transmitters are two different acoustic sources. The monopole transmitter is an omnidirectional sound energy source that emits sound waves in all

directions around it. Dipole acoustic sources, which are nonaxisymmetric sources, generate sound waves in one direction. The monopole source generates body waves that travel in the body of the formations; the dipole source generates surface waves that travel on the borehole wall. Each one of these two types of waves includes different types of waves (Close et al., 2009). Most of these waves are presented in **Fig. 11.**

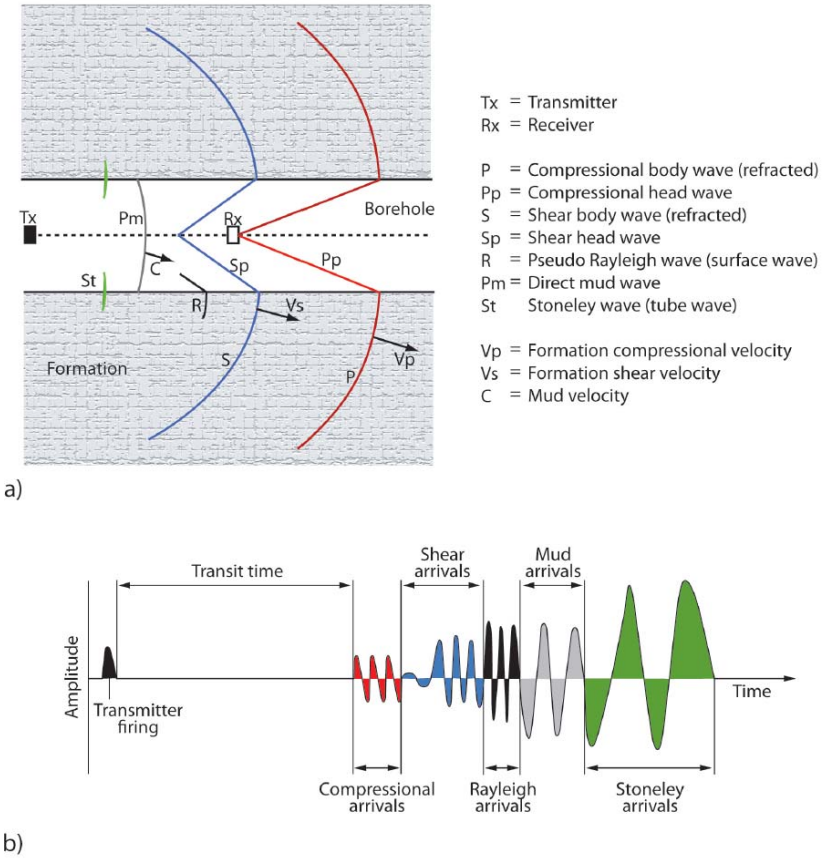

Fig. 11—A. Important sonic waveform component propagation in a borehole as the P wave energy is detected. B. Schematic of the wavetrain detected at the receiver as a function of time (Close et al., 2009)

2.3 Fast Compressional Waves

Fast compressional waves are the primary P-waves, which are the fastest waves and are seen at the beginning of the waveform. Monopole and dipole sources both can generate P-waves. However, a P-wave generated from a dipole source is not detectable with most processing techniques. A P-wave is not dispersive, which means its velocity does not change with changing frequency (Crain and Eng). This kind of wave propagates parallel to the direction of particle motion **(Fig. 12)**.

2.4 Slow Compressional Waves

Slow compressional waves do not appear in the wave train because their amplitudes decay and the waves transfer to heat before being detected. Slow compressional waves were predicted by Biot in 1952 and detected by Johnson and Plona in 1982. There is no known application for them in the oil industry yet (Crain and Eng 2004).

2.5 Surface Compressional Waves

Surface compressional waves is another name for leaky compressional waves, so called because some of the borehole P-wave energy is lost and converted into shear waves that radiate away from the borehole. Leaky P-waves are generated by monopole sources in slow formations and appear in the waveform after the compressional waves and before the shear waves as ringing. Leaky P-waves are dispersive waves; they are close to the formation P velocity at the low frequency and approach fluid velocity at high frequency (Close et al., 2009; Crain and Eng).

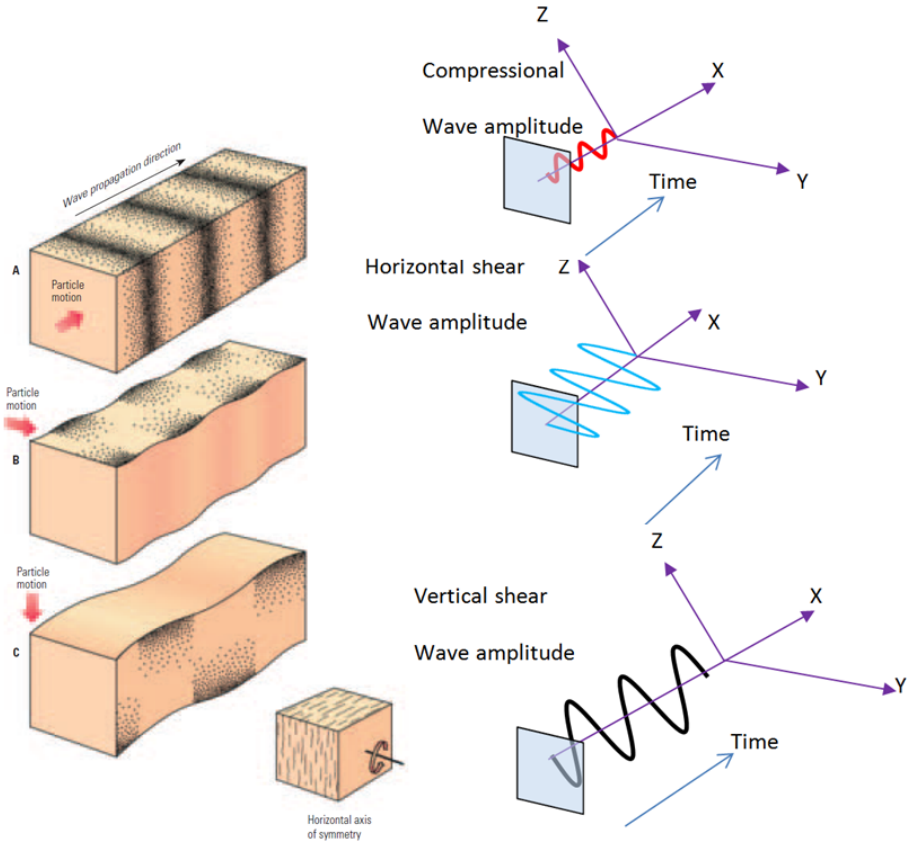

Fig. 12—In the case of compressional wave propagation, particles move in the direction of wave propagation. In the case of shear wave propagation, particles move orthogonal to the direction of wave propagation (Haldorsen et al., 2006).

2.6 Shear Body Waves

Shear body waves are also called secondary waves. They are slower than body compressional waves and they appear after the compressional wave in the wave train. Their amplitude is much higher than the amplitude of the compressional wave. S-waves do not travel in fluid and can be generated from the conventional monopole source only

in fast formations where their velocity is higher than mud velocity ($V_s > V_f$). In slow formations, S-wave velocity can be determined either indirectly or directly. The indirect methods estimate S-wave velocity from the P-wave or Stoneley wave. The direct methods use dipole acoustic sources to generate flexure waves, which have the same velocity as S-waves. Flexure waves are dispersive and their low-frequency component velocity equals the formation shear wave velocity, and their high-frequency component velocity equals fluid velocity (Crain and Eng). Shear waves propagate perpendicular to the particle motion direction **(Fig. 12).**

2.7 Shear Surface Waves

Shear surface waves are also called pseudo-Rayleigh waves because they have the same motion of the surface Rayleigh wave, but they are found in the borehole. Pseudo-Rayleigh waves are generated by monopole sources only in fast formations. They are dispersive; their low-frequency dispersion has the same velocity as shear waves, and their high-frequency component velocity is close to the fluid velocity (Crain and Eng).

2.8 Stoneley Waves

Stoneley waves are slow, guided waves that travel on the surface of the borehole. Stoneley waves are generated by monopole sources and their motion of propagation is described as piston-like (**Fig. 13**). They are used to detect fractured and permeable zones because they lose energy passing through these zones. The low-frequency components of Stoneley waves are called tube waves (Haldorsen et al., 2006).

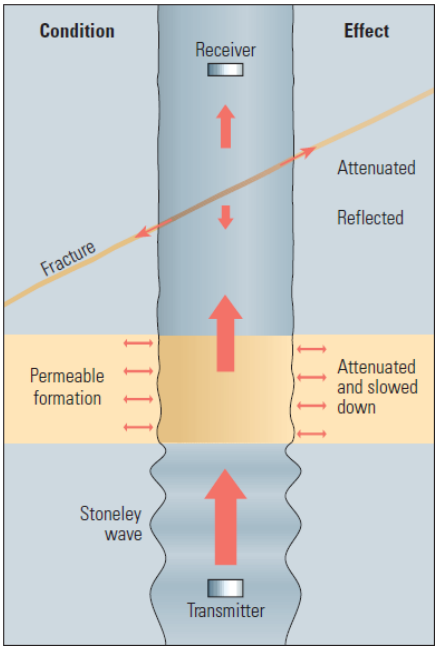

Fig. 13—The Stoneley waves have a piston-like movement and travel on the surface of the borehole. The Stoneley waves push fluid into formation at permeable zones and fractures (Haldorsen et al., 2006).

2.9 Fluid Waves and Direct Waves

Fluid waves are the compressional waves that travel from the monopole transmitter to the receiver through the borehole fluid. Direct waves travel from the transmitter to the receiver through the body of the logging tool (Crain and Eng).

CHAPTER III

SINGLE-WELL ACOUSTIC MIGRATION IMAGING LITERATURE REVIEW

3.1 Chronological Study of Single-Well Imaging Work

Several techniques have been tried for single-well imaging using full waveforms of acoustic logging. Over the years the techniques have been improved; in the effort to provide a deeper single-well acoustic image around the borehole. These techniques include using different logging tool geometries, different transmitters, and different filtering and image migration methods.

Hornby's (1989) work is considered as the starting point for reviewing the development of using full-waveform sonic data for imaging of near-borehole structures. His work appears to be the first to apply surface seismic migration to borehole sonic data. Secondary arrival, which is reflected by structural features around borehole is contained in the full waveform record by an array of receivers. Using the same principle of seismic migration, Hornby used the secondary arrivals to generate an image of the structural features around the borehole. The tool he used was an experimental acoustic well-logging tool equipped with a single monopole and 12 receivers. His processing consisted of two main steps. First, he removed direct P and S head waves and Stoneley waves using a frequency/wavenumber domain (f-k) filter. Then, he separated upgoing and downgoing data using the "backprojection operator" migration algorithm. Hornby

was imaged features 18 m away from the borehole, but he did not apply any static correction or deconvolution to the data (Hornby, 1989).

Fortin et al. (1991) used conventional seismic processing to generate images away from the borehole in a deviated well with an Evaluation of Velocity and Attenuation (EVA) array sonic logging tool that consists of four transmitters and 12 receivers. Any transmitter can be combined with any receiver, thus giving 48 possible offsets. After removing the unwanted waves using high-cut and low-cut filters, Fortin at el. separated reflections from above and below the well axis and generated two images. Finally, they combined the two resulting sections together along their zero line, which, in the representation, became the well axis. Doing that, they imaged features to 7 m away from the borehole. Their processing flow left considerable room for improvement that remains in all the other available processes, such as deconvolution and static correction. Migration was not used in this processing-imaging flow.

Yamamoto and Watanabe (2000) attempted imaging in Oman in a horizontal well using a modified multireceiver sonic tool. The spacing between transmitter and receiver was extended more than for the conventional tool. Four different waveforms were recorded at each receiver station. The processing techniques used the four waveforms to separate reflections from below and above the well. After removing the unwanted waves such as P and S, they used a migration algorithm to move reflected waves into the true position

relative to the borehole. The resulting image had a range of 3 to 13 m (Yamamoto et al., 2000).

In their test site in Mounds, Oklahoma, Li et al. (2001) used a pilot acoustic reflection survey (ARS) in a deviated well to produce single-well imaging (SWI). ARS uses one transmitter and eight receivers to image structural features 9 m 30 ft away from the borehole. The tool they used was an XMAC (Elite) tool, which has an eight-receiver array and one transmitter with a receiver spacing of 0.5 ft The data processing procedure was done in sequential steps. The first step was to apply a median filter to reject direct arrivals. Then, they used an FK filter to separate the upgoing and downgoing reflected waves. Next, they enhanced the downgoing and upgoing reflections. Finally, they used Kirchhoff depth migration to obtain the formation image in depth. The result was imaging formation boundaries outside a wellbore up to 15 ft The analysis of this data set shows that the image range and resolutions depend on the dip of the well trajectory.

In previous work, Tang (2004) used compressional waves generated by a monopole source. The problem was that the monopole data is insensitive to direction of the reflector since the source emits acoustic waves in all directions. The work was taken a step ahead by using compressional waves generated from a dipole source to determine reflector orientation. He used a directional acoustic measurement tool of low-frequency content (about 2 to 3 kHz). The low frequency range allowed Tang to image the radial extent of the formation structure up to 15 m. Monopole compressional waves with a

center frequency of about 8 to10 kHz are commonly used for this imaging. The migration of the acoustic data of each component for imaging a formation structure uses the conventional seismic processing method. Tang had to solve the problem of tool rotation while logging to be able to determine reflector orientation. To do that, the directional acoustic data were acquired with an acoustic logging tool in a borehole and record the azimuth (AZ) of the tool relative to a fixed coordinate such as earth's north. Then, he converted the multiple-component data into the fixed coordinates. Generating the image from the rotated data begin with separating the reflected arrivals from the direct arrivals based on their moveout characteristics. Then, he separated the downgoing and upgoing reflection events. Migration was then applied to image the upper and lower sides of the formation reflector. After migration, acoustic component data were mapped into a two-dimensional (2D) domain. One dimension is the radial distance, *r*, away from the borehole axis; the other is *z*, the logging depth or the tool position, along the borehole. Compared to the monopole result, the dipole result shows a clearer and better image of bed boundaries, the radial extent reaching 50 ft into the formation. Although the bed boundaries on the monopole image appear to have a higher resolution, they have a limited radial extension (approximately 12 ft in this case). This significantly enhanced depth of penetration using dipole data because of the low-frequency or long-wavelength nature of the data.

CHAPTER IV

ANISOTROPY ESTIMATION METHODOLOGIES

Geophysical measurements are frequency dependent. The depth of investigation and the volume of rock being evaluated get larger as the measurement working frequency range gets lower. Trying to understand the causes of the water encroachment and effects of fractures in the west flank of Harahd field, I compared results from two different geophysical methods of different scales. The two methods are the vertical seismic profile (VSP) and single-well acoustic impedance imaging (SWI). The VSP provides measurements at low frequency range and large wave length. That enables evaluating large volumes of rock and characterization of major subsurface features such as large faults. The depth of investigation of the VSP is around 100 to 1,000 ft On the other hand, the SWI working frequency range is higher, so it evaluates a smaller volume of rock at a depth of investigation in tens of feet. Beside the previous two main methods, the cross-dipole measurement, recorded and processed by Baker Hughes, is available as supportive wireline log data for the study. The cross-dipole measurement works at very high frequency and its depth of investigation is between 2 and 4 ft.

The results and VSP data were provided to me by Saudi Aramco to compare with the results of the SWI I processed using Baker Hughes's image processing software. A detailed discussion of the used VSP processing steps can be found in the literature (Owusu et al., 2009).

4.1 Vertical Seismic Profile

In quasi-P (qP-wave) mode, anisotropy yields a little coupling of shear vibration to compressional wave. Similarly, anisotropy produces a small coupling of compressional vibration to shear wave in quasi-S (qS-wave) mode. These modes are necessary to solve some complicated stress-strain relations (Paillet and Cheng, 1991). In our case, quasi modes are included in the raw VSP data and can be used to determine fracture(s) orientations(s) using three different methods: azimuthal qP-wave traveltime, amplitude, and polarization. Fractures can be related to anisotropy when they are small enough to be comparable to wavelength. Elliptical fitting was used in all the three analyses to compute anisotropy degree. In the least-squares elliptical fitting, the data is plotted with respect to direction, and the best ellipse to fit the data is plotted (**Fig. 14)**. When qP-waves travel in the same direction as fracture strike, it will show smaller traveltime and higher amplitude compare to qP-waves that travel perpendicular to the fracture-strike direction. Knowing that, anisotropy can be calculated from the ratio of the short axis (B) to the long axis (A) of the ellipse. (Owusu et al., 2009):

$$\text{Anisotropy} = (1 - B / A) \times 100. \quad \text{.....} \quad 4.1$$

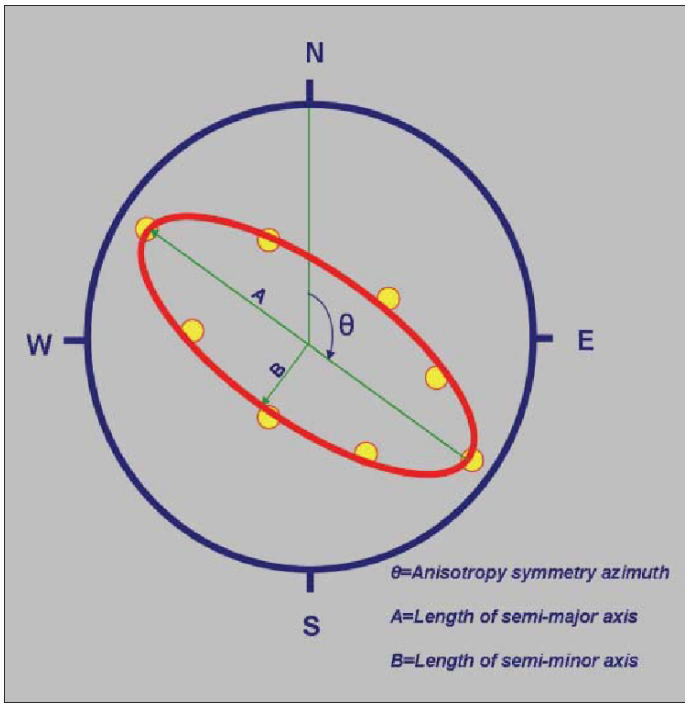

Fig. 14—A schematic sketch of fitting a least-square ellipse to the measured data (Owusu et al., 2009)

Elliptical shape is generated for every kind of VSP data (traveltime, amplitude, and polarization angle) at every geophone depth level. For each of the three types of data, a rose plot can be constructed to indicate the most dominant anisotropy direction indicated by that kind of data. A rose plot for a specific interval or formation is generated by staking all the elliptical shapes fitted for the geophones within that interval. The rose plot will indicate the most dominate anisotropy direction, but if no anisotropy is indicated in a specific direction, data still exist in that direction. In this project, the data was used to construct the elliptical shapes which then form the rose plots (**Fig. 15**).

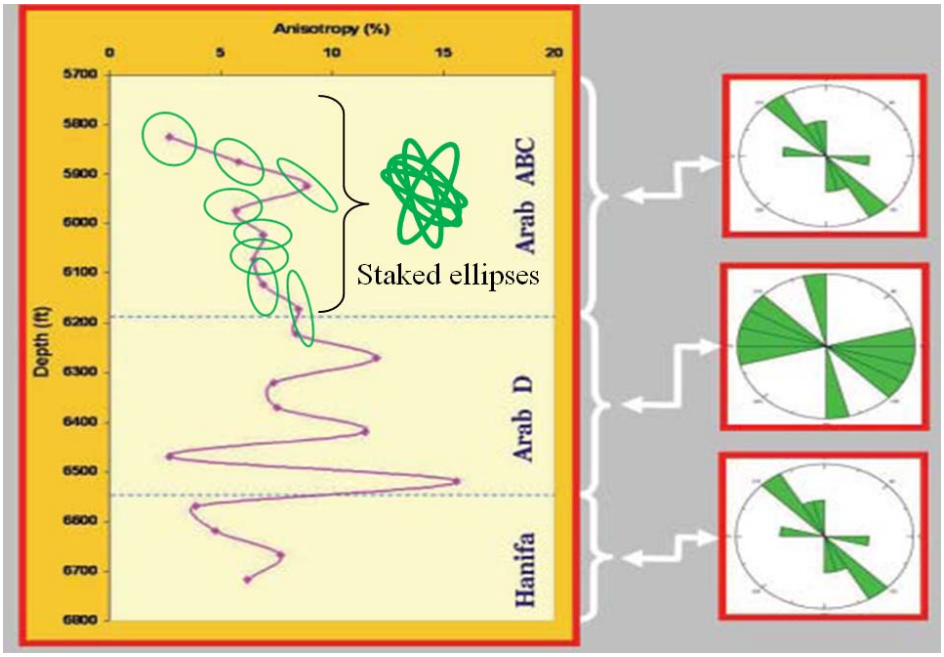

Fig. 15—Fitting elliptical curves to the VSP data using the least-squares ellipsoid is fitted to the data. Ellipses fit to the data measured at every receiver (left side) show how, and how several ellipses are stacked on the top of each other for on depth interval to generate rose plots on the (right side) The ratio between the long and short axis of the ellipse is used to calculate the degree of anisotropy at depth level for every receiver (Owusu et al., 2009).

4.1.1 VSP Acquisition System

Multilevel walkaround VSP acquisition systems have been used to perform seismic measurements. The surveys consist of a number of shot points on the surface with equal separation distance and azimuthal degree arranged in a circle around the studied wellbore. 3-C geophones are placed inside the wellbore at different levels (depths) (**Fig. 16**). Every time a source on the surface is fired, the data are recorded on the receivers on all the levels (Owusu et al., 2009).

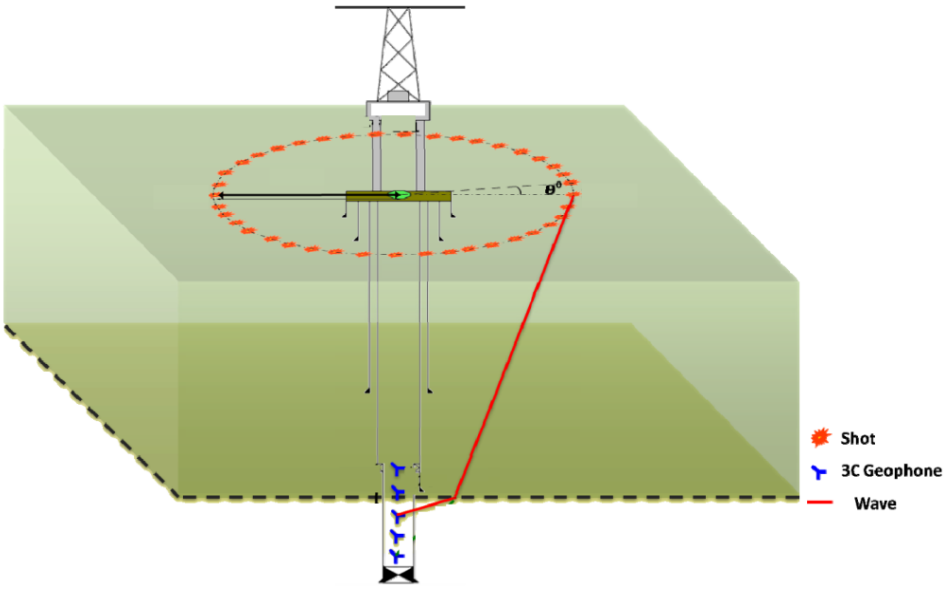

Fig. 16—A sketch of a VSP system where shots are placed in a circle around the borehole with θ° separation intervals between each two consecutive shots. 3-component geophones are placed at different depths inside the borehole (Dulaijan et al., 2011)

4.1.2 Azimuthal Variations of the Transmitted qP-Wave Traveltime

The traveltime azimuthal variation is directly affected by fracture orientation. Waves travel slower in unconsolidated materials than in consolidated materials. Because of that, waves traveling in the same direction of the fracture-strike orientation will have shorter traveltime than waves traveling perpendicular to fracture-strike orientation. That is the base to calculate anisotropy using the least-squares ellipse fitting method. The data collected from geophones are plotted on a rose diagram, and the shorter axis of the ellipse will indicate the fracture strikev **(Fig. 17)** (Owusu et al., 2009).

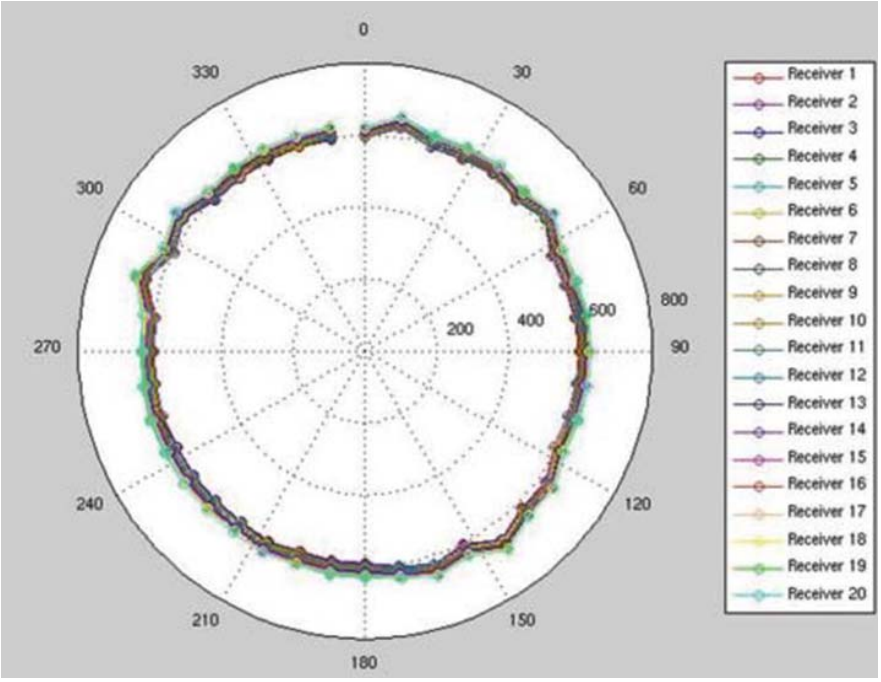

Fig. 17—Traveltime data masured from 20 receivers and ploted on the top of each other

4.1.3 Azimuthal Variations of the Transmitted qP-Wave Polarization Angle

Polarization is the particle displacement vector that describes the particle motion in three dimensions at a given point in space (Anderson and Nehorai, 1996). One way to determine the particle displacement created by a linearly polarized compressional wavelet is to construct hodograms from the responses recorded by 3-C geophones (Hardage, 2000). To create a hodogram, wave amplitudes recorded by two of the three geophone components are plotted against each other at any specific time (t) located within the time window from T1 to T2. The setting of the 3-C geophone which is being discussed here is one with the vertical component on the longitude axis and all the three

components orthogonal to each other **(Fig. 18)**. The incident angle θ that is measured from the vertical axis can be found by plotting the wave amplitude recorded by the vertical Z-geophone versus the wave amplitude recorded by the horizontal X-geophone. In the same way, wave amplitude recorded by the horizontal Y-geophone can be plotted versus the wave amplitude recorded by the horizontal X-geophone to find the azimuth angle Φ. If the horizontal X-geophone orientation relative to north is known then, azimuth angle Φ relative to north can be determined.

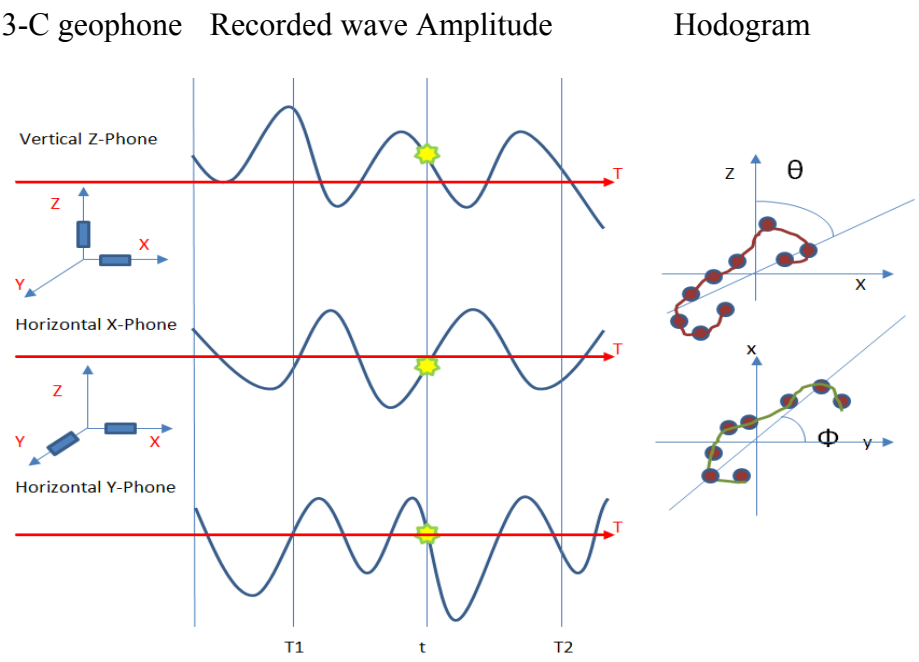

Fig. 18—A schematic representation of wave amplitudes (middle) recorded by 3-component geophone (left) and two hodograms (right). The hodogram on the top resulted from plotting wave amplitude using data from the vertical Z-geophone versus the data from the horizontal X-geophone to estimate the incident angle θ° that is measured from the vertical axis. The hodogram at the bottom resulted from plotting wave amplitude using data from the horizontal X-geophone versus the data from the horizontal Y-geophone to estimate the azimuth angle Φ°

The multicomponent geophone arrays tend to twist about the vertical axis when moved up or down inside the borehole. In most VSP experiments, the horizontal orientation of the receivers is unknown because without gyroscopic information, the orientation of the horizontal geophones (X and Y) cannot be determined. For this reason, polarization is parameterized by the incident angle measured from the vertical axis (Weber et al., 2011). The orientation of the horizontal geophones can be estimated by analyzing the particle motion of each component. For nonzero offset VSP surveys, the process involves a series of mathematical rotations about different component axes to align the vertical Z-geophone and one of the horizontal geophnes in the plane that contain the particle displacement vector created by the first arrival of the direct, downgoing P-wave. The downward wave field contains particle displacements polarized in the direction of the first arrival P-wave, vertical S-wave (SV) and horizontal S-wave (SH). The first mathematical rotation is about the vertical Z-geophone axis to rotate the horizontal X-geophone toward a vertical plane from the borehole to the source to generate radial component. The second rotation is done about the horizontal Y-geophone horizontal axis. This tilts the X-geophone toward the vertical axis to point directly at the source. The incident angle measured from the vertical axis generated from the second rotation is the one the Saudi Aramco study called it the polarization angle (Owusu et al., 2009). In anisotropic formations the vertical angle will show a marked change from one source position to another. Data from the polarization step (second rotation) are analyzed for elliptical anisotropy in the same manner as the traveltime data.

4.2 Anisotropy Estimation from Cross-Dipole Measurements

Another method to estimate formation anisotropy is from the cross-dipole measurements. Axis of symmetry is the perpendicular axis to the plane where the medium properties are independent of the direction around that axis. Transfer isotropic media (TI) are asymmetric anisotropy systems, where the properties are the same only around the axis of symmetry, not along another axis. Horizontal layers form anisotropic medium along the vertical axis of symmetry, but each layer forms isotropic plane perpendicular to the vertical axis of symmetry. That configuration is called transversely isotropic with a vertical axis of symmetry (TIV). Aligned vertical fractures create an anisotropic medium along the horizontal axis of symmetry and isotropic planes perpendicular to the horizontal axis of symmetry. This medium is known as transversely isotropic with a horizontal axis of symmetry (TIH) (**Fig. 19**) (Close et al., 2009).

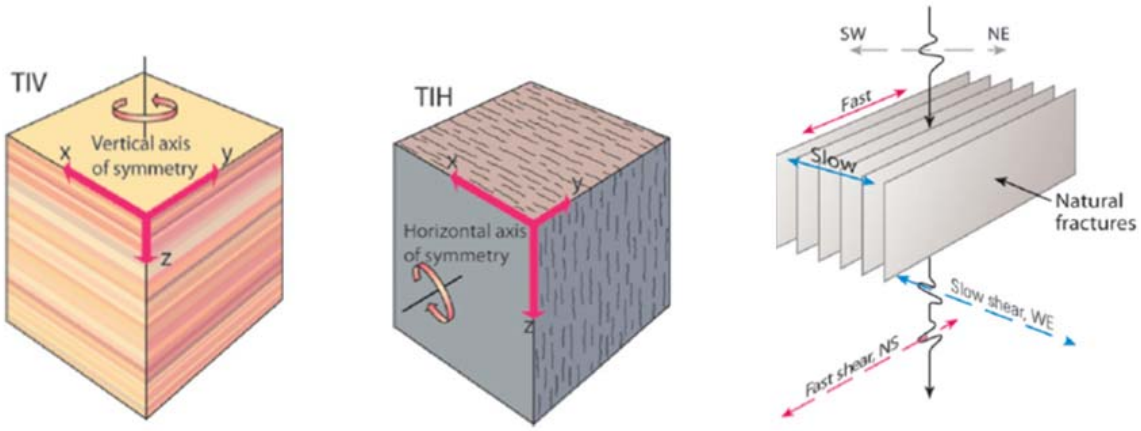

Fig. 19—Schematic representation of vertical transverse isotropy rock (TIV) and Horizontal transverse isotropy rock (TIH). Layered formations form TIV and fracture formations form TIH (Close et al., 2009).

4.3 Acoustic Impedance Imaging Around Borehole Using S-Wave Dipole Data

Using shear waves generated from dipole sources as a tool to image geological features away from the borehole is high-end dipole acoustic data processing. The latest technique is the one used by Tang and Patterson (2009). As discussed in Chapter III, acoustic imaging has developed over the years since Hornby attempted it in 1989. The breakthrough was in 2007 when Tang et al. used the dipole shear wave and took advantage of its directional sensitivity to determine near-wellbore geological feature orientation. Before that, acoustic imaging was done using compressional waves generated by a monopole source, which cannot be used to determine the orientation of the subsurface features around the wellbore. Tang et al. (2007) used a compressional wave generated by a dipole source to determine the subsurface feature's azimuth, but compressional waves from a dipole can be generated exclusively in slow formations. Tang and Patterson is new processing technique was applied to directional acoustic data acquired using a 4-C cross-dipole acoustic logging tool to obtain an image and azimuthal information about near-wellbore features. This processing technique consists of a chain of processing steps:

1. Correct for tool rotation while logging
2. Perform data deconvolution
3. Apply the Tang et al. (2007) reflection signal processing technique to single inline data to gain reflection signals from geological feature imaging (Tang and Patterson, 2009).

The Baker Hughes processing package software called eXpress uses these processing steps for imaging features around the borehole. eXpress was used to apply imaging processing to the field data of this study. The following sections will explain and demonstrate the theories behind the steps used in used the eXpress software.

4.3.1 Correct for Tool Rotation While Logging by Converting the 4-C Data to Fixed Coordinates

Dipole acoustic measurements depend on their direction of measurement. That means the transmitted and received wave amplitudes change with respect to the angle α between the receiver or the source direction and the particle motion direction as (Tang, 2004):

$$\text{Amplitude} = A_0 \times \text{Cos}\ \alpha. \quad \text{4.3}$$

where A_0 is wave amplitude at α = 0°. Because of that, the data must be converted from the changing tool azimuth to a fixed coordinate. Tool azimuth A is usually recorded while logging with respect to the earth's north. The recorded tool azimuth A can be used then to convert acoustic data into a fixed coordinate. Shear waves transmitted by 4-C cross diploe tool decompose into a vertical shear component (SV) and a horizontal shear component (SH) **(Fig. 20)**. The in-line and cross-line recorded data can be defined mathematically by SV, SH and the changing tool azimuth with respect to bedding plane Ø as (Tang and Patterson, 2009):

$$xx = SH\ \text{X}\ \text{Cos}^2 ø + SV\ \text{X}\ \text{Sin}^2 ø. \quad \text{4.4}$$

$$xy = -\ SH\ *\ \text{Sin}\, ø\ \text{Cos}\, ø + SV\ *\ \text{Sin}\, ø\ \text{Cos}\, ø. \quad \text{4.5}$$

$$yy = SH \text{ X } \text{Sin}^2 \text{ø} + SV \text{ X } \text{Cos}^2 \text{ø} \text{.....} \quad 4.6$$

$$yx = - SH \text{ X } \text{Sin ø Cos ø} + SV \text{ X } \text{Sin ø Cos ø}. \text{.....} \quad 4.7$$

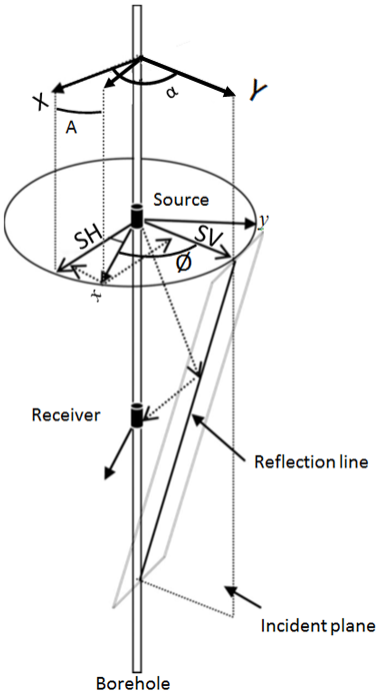

Fig. 20— Using a 4-C cross-dipole acoustic wieline tool in the borehole to record reflected SV-waves and SH-waves from an inclined reflector. SV-waves toward the reflector are generated by projecting an x-dipole source along the wave incident plane. The generated SH-waves are orthogonal to that plane. The reflected SV- and SH-waves are projected onto the x- and y-dipole receivers. The recorded data can be converted to fixed coordinates X-Y (Tang and Patterson, 2009).

Consider the tool coordinate x-y and a fixed coordinates X-Y in Fig.20. The X-axis makes angle α with the bedding plane. The tool x-axis has an azimuth A with respect to

the fixed coordinate X-axis. At the same time, the tool makes *Ø* changing azimuth with respect to the bedding plane. This relation between angles can be written as:

$\alpha = A + \phi$. 4.8

This makes it possible to use A to convert the 4-C component in-line and cross-line data from the tool coordinate x-axis and y-axis to a fixed coordinate X-axis and Y-Axis as (Tang, 2004):

$$\begin{aligned} XX &= xx\cdot\cos^2 A-(xy+yx)\cdot\cos A\cdot\sin A+yy\cdot\sin^2 A \\ XY &= (xx-yy)\cdot\cos A\cdot\sin A+xy\cdot\cos^2 A-yx\cdot\sin^2 A \\ YX &= (xx-yy)\cdot\cos A\cdot\sin A+yx\cdot\cos^2 A-xy\cdot\sin^2 A \\ YY &= yy\cdot\cos^2 A+(xy+yx)\cdot\cos A\cdot\sin A+xx\cdot\sin^2 A \end{aligned} \quad \text{..... 4.9}$$

This will maintain the 4-C components with respect to reflector azimuth in the fixed coordinate regardless of tool rotation. These fixed-coordinate 4-C components now can be used to estimate reflector azimuthal α. This is done by using the fixed coordinate 4-C components to for a new cross-line component (Eq. 4.10). The value of α that minimizes the new cross-line component is the reflector azimuth with respect to the fixed coordinate (Tang and Patterson, 2009).

$$\begin{aligned} XY' &= (XX-YY)\cdot\cos\alpha\cdot\sin\alpha+XY\cdot\cos^2\alpha-YX\cdot\sin^2\alpha, \\ YX' &= (XX-YY)\cdot\cos\alpha\cdot\sin\alpha+YX\cdot\cos^2\alpha-XY\cdot\sin^2\alpha. \end{aligned} \quad \text{..... 4.10}$$

4.3.2 Data Deconvolution

The 4-C processing method explained in the previous section was applied using eXpress at the same step of deconvoluting the data. The three important results from the deconvolution step are:

1. reducing wave data ringing
2. improving later arrivals by applying attenuation compensation
3. Performing 4-C dipole data deconvolution and rotation

The program applies the Wiener deconvolution method to suppress the unwanted ringing of acoustic waveform data. To do so, the first-arrival portion of the wave is selected as the desired wavelet. Then the wave data are matched to the first portion of the wavelet to construct the deconvolution filter to minimize the ringing in the waveforms. Using deconvolved data in producing an acoustic image improves the resolution of the acoustic reflection imaging result. Attenuation compensation can also apply to the data to enhance reflected waves in the later portion of the data. Attenuation compensation is done by taking into account the rock quality value (Q). Rocks with high Q values preserve more wave energy than rocks with low Q values. Usually the value entered into the program is between 1 and 4. High values may boost waves of high energy, and masking the reflected waves of low energy makes it difficult to image reflectors. Deconvolution can also be applied to the 4-C dipole data and also can be rotated by entering the tool azimuth curve as one of the inputs. The angle of rotation can be changed by subtract or add the required degrees from the original tool azimuth.

4.3.3 Reflection Signal Processing and Image Migration

The Tang et al. (2007) reflection signal processing technique is incorporated in the eXpress package. This technique is mainly two steps. The first step is to separate the direct and reflected waves. The second step is to separate the reflected waves into upgoing and downgoing reflected waves.

The full waveform (W) contains both the direct waves (D) and the reflected waves (R). In the first step, the reflected waves are extracted from the full waveform by subtracting the direct waves from the full wave form. The residual waves from the subtraction are the reflected waves as (Tang et al., 2006):

$$R = W - D \quad \text{..... 4.11}$$

The direct waves must be estimated to subtract them from the full waveform. The direct wave propagation is described by (Tang et al., 2007):

$$A_l(\omega)\ e^{\wedge}(l\omega z/V_1), (l = 1, \ldots, L) \quad \text{..... 4.12}$$

where ω is angular frequency and L is the number of direct waves in the array of size N. The unknown wave mode amplitude spectrum $A_l(\omega)$ is related to the spectral array data $W(n)$, ($n = 1, \ldots N$) via the following matrix equation:

$$n\text{th row} \rightarrow \begin{bmatrix} E_1^{1-n} & \cdots & E_L^{1-n} \\ \vdots & & \vdots \\ E_1^{0} & \cdots & E_L^{0} \\ \vdots & & \vdots \\ E_1^{N-n} & \cdots & E_L^{N-n} \end{bmatrix} \begin{bmatrix} A_1(\omega) \\ \vdots \\ A_L(\omega) \end{bmatrix} = \begin{bmatrix} W_1(\omega) \\ \vdots \\ W_n(\omega) \\ \vdots \\ W_N(\omega) \end{bmatrix}. \quad \text{..... 4.13}$$

where El [is] the propagation exponential $\exp(i\omega z/v_l)$.

The least square solution for A can be found by:

$$\mathbf{A} = (\tilde{\mathbf{E}}^T \cdot \mathbf{E})^{-1} \cdot \tilde{\mathbf{E}}^T \cdot \mathbf{W} \quad \ldots\ldots\ldots\ldots 4.14$$

where ~ denotes taking a complex conjugate and T denotes transpose (Tang et al., 2007).

Then the extracted reflected waves are separated into upgoing and downgoing reflected waves based on the position of the tool relative to the geological feature. If the tool is below the geological feature, downgoing reflected waves are recorded. If the tool is above the geological feature, upgoing reflected waves are recorded. Mathematically, it can be expressed using Snell's law as (Tang et al., 2007):

$$T = \begin{cases} \dfrac{\sqrt{z^2 + 4Z(Z-z)\sin^2\alpha}}{v_1} & \text{(tool below bed)} \\ \dfrac{\sqrt{z^2 + 4Z(Z+z)\sin^2\alpha}}{v_2} & \text{(tool above bed)}, \end{cases} \quad \ldots\ldots\ldots\ldots 4.11$$

where, α is the angle between borehole and bed boundary, Z is the distance between the acoustic source and the bed intersection with the borehole, and z is the distance between the source and one of the array receivers. A wave moveout is the derivative of time with respect to distance. The reflection moveout from Eq. 4.11 is (Tang et al., 2007):

$$\frac{dT}{dz} = \begin{cases} \dfrac{z - 2Z\sin^2\alpha}{v\sqrt{z^2 + 4Z(Z - z)\sin^2\alpha}} = \dfrac{z - 2Z\sin^2\alpha}{v^2T} & \text{(tool below bed} \\ \dfrac{z + 2Z\sin^2\alpha}{v\sqrt{z^2 + 4Z(Z + z)\sin^2\alpha}} = \dfrac{z + 2Z\sin^2\alpha}{v^2T} & \text{(tool above bed} \end{cases} \quad \ldots\ldots\ldots\ldots 4.12$$

The moveout sign changes from positive to zero then negative as the tool approaches the bed boundary from below while logging because *Z* gets smaller as the tool gets closer to the boundary. On the other hand, the sign of the moveout when the tool is above the boundary is always positive because *Z* gets larger as the tool moves away from the boundary **(Fig. 21)**.

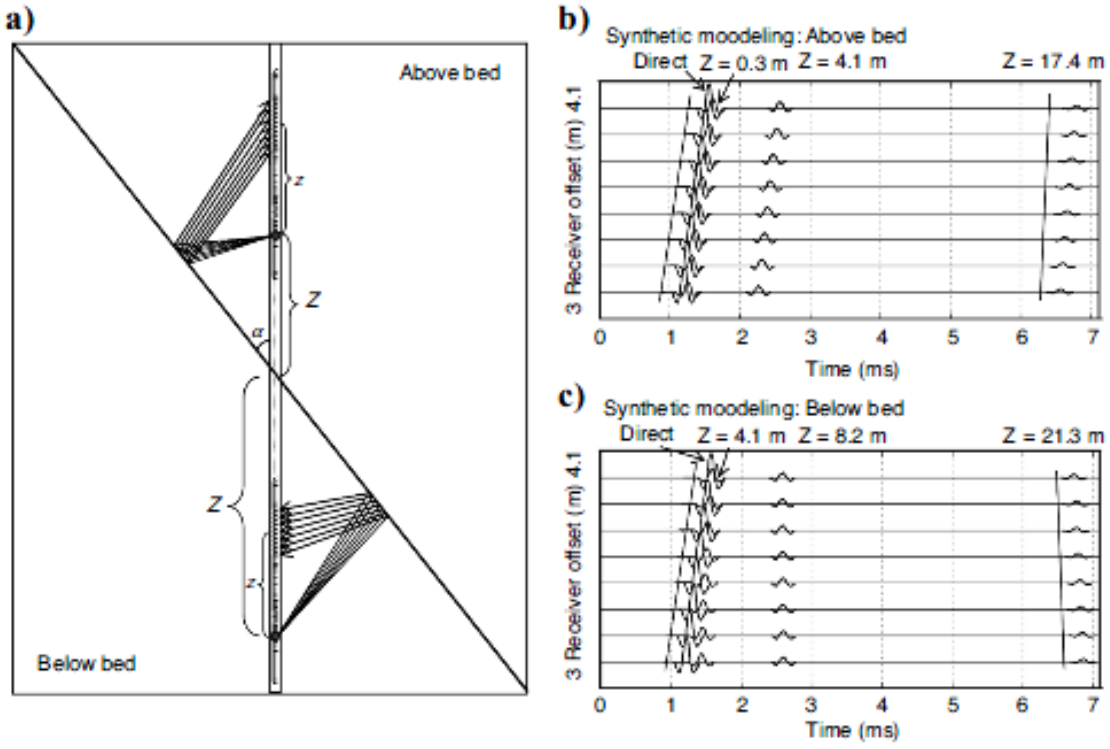

Fig. 21—(a) Wireline acoustic tool position with respect to a near-wellbore bed boundary and downward reflected waves when the tool is below the bed boundary (bottom) and upward reflected waves when the tool is above the bed boundary. (b) and (c) show the different reflection moveouts when the tool is below or above the bed (b) scenarios (Tang et al., 2007).

Finally, after doing all the above steps, the data is migrated from the time domain to the distance domain. There are different migration methods to do this job. The one used by eXpress is the Kirchhoff migration method (Tang et al., 2007). The shear wave velocity of the investigated formation must be known to perform migration from time to the distance domain and to find how far the reflector is from the borehole. For our field data, shear wave velocity was used to perform migration with the shear wave velocity

estimated from the dipole shear logging data. Migration done by eXpress will generate two images, one image is for the upgoing reflected waves and the other one is for the downgoing reflected waves. Putting both images next to each other allows user to visualize reflectors as if they are crossing the borehole.

CHAPTER V

RESULTS AND DISCUSSION

To understand the problem of the premature water coining in the west flank of Haradh field, VSP and different wireline log measurements were recorded in two observation wells in the area of study. The following sections demonstrate and discuss those results. Some important information must be taken in consideration before discussing the results:

- The studied area is a highly fractured area with three defined fracture orientations (N130E, N80E and N20E).
- The oil/water contact in the west flank is 800 ft higher than in the east flank.
- Water in the west flank is younger and fresher (30,000 ppm TDS) than water in the east flank (150,000 ppm TDS).
- Haradh field forms a simple, shallow, asymmetrical anticline with a steeper western flank and it dips between 3° and 8°.
- The maximum stress direction is varies between N50E and N90E **(Fig. 22).**

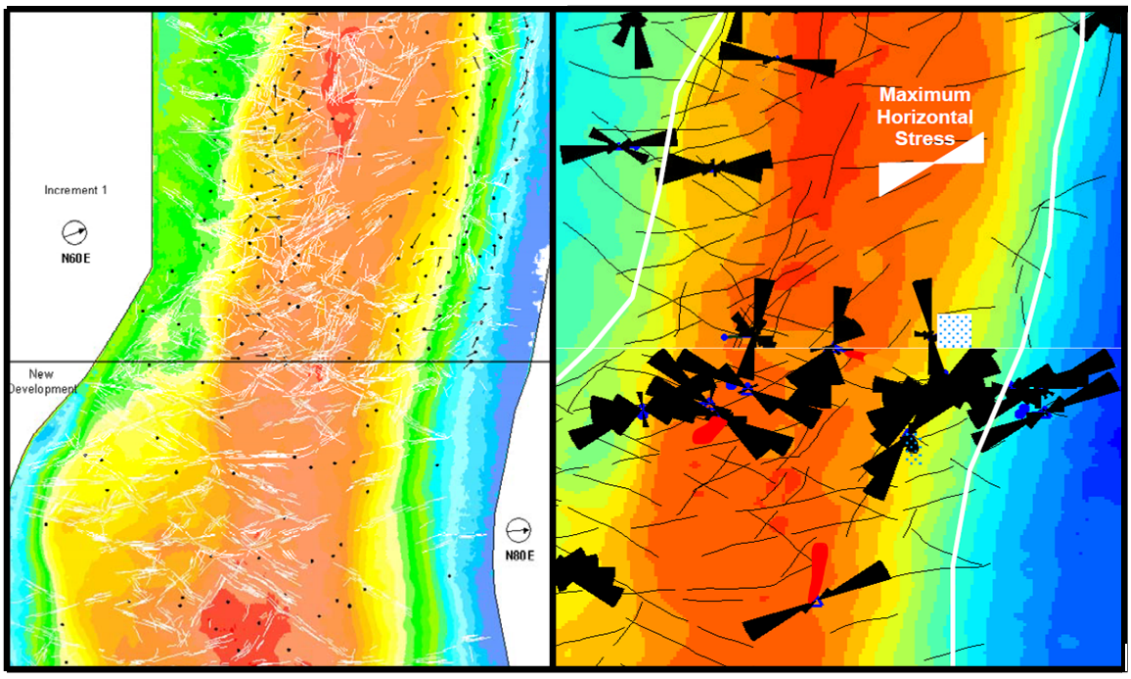

Fig. 22—Haradh field fracture map (left) and the maximum horizontal stress direction (right) (Bu-Hulaigah et al., 2001; Stenger et al., 2002)

5.1 Measurements Result from the Uninvaded Well

5.1.1 VSP Recording Setting in the Uninvaded Well

Trying to understand the root cause of the unexpected flooding behavior, a walkaround VSP was acquired in the offset well drilled in the same formation. Forty equidistant source points in the VSP survey were located along a circle at an off set of 1000 m from the wellhead. The angular increment was 9° **(Fig. 23a)**. The receivers were in a 20-level, 3-C receiver array and spaced at 50-ft intervals over the depth range from 5,800 ft to 6,742 ft **(Fig. 23b)**.

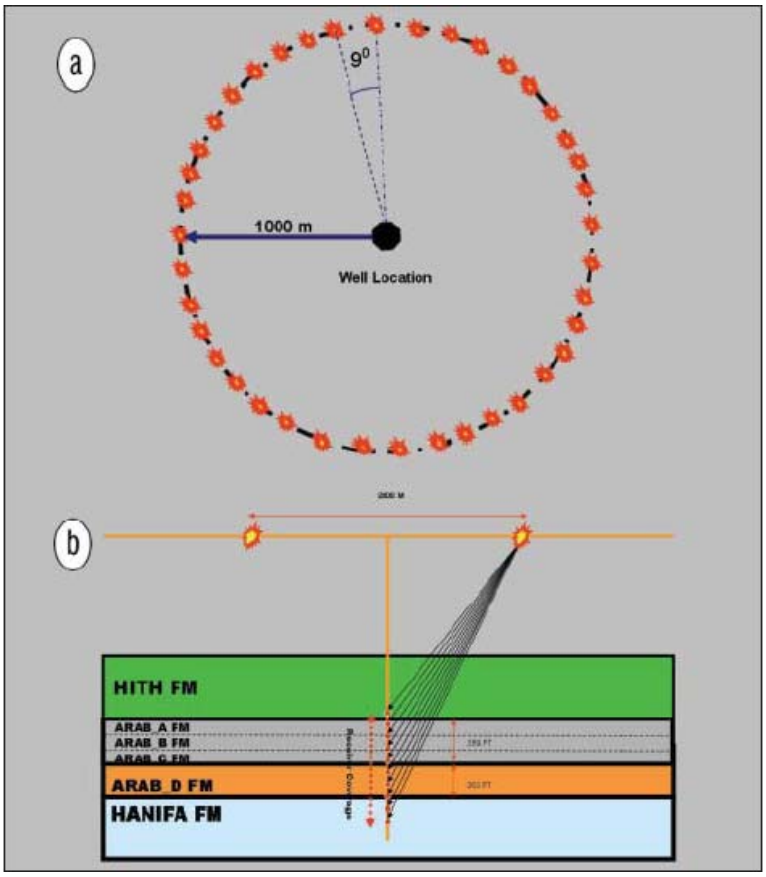

Fig. 23— (a) Top view of the walkaround VSP survey show the distance between transmitters and receiver and separation between transmitters. (b) A cross-section of the well shows the receiver configuration for the walkaround VSP survey at 20 different depth levels inside the well. The separation between any two consecutive 3-C receivers is 50-ft intervals. The top depth of the evaluated interval is 5,800 ft and the bottom is 6,742 ft (Owusu et al., 2009).

5.1.2 Result Discussion

The first data set was recorded in the uninvaded observation well. The well was drilled and completed as a vertical openhole observation oil well, across a limestone reservoir on the west flank of an oil field. A surface map shows the locations of the two wells in

the area of study, where an irregular water encroachment was detected **(Fig. 24)**. Also, the map shows the actual (solid line) and modeled (dashed line) waterflooding and five rose plots that resulted from VSP, formation microimaging (FMI) and dipole sonic imaging (DSI). Water moves toward the well in the NW-SE direction.

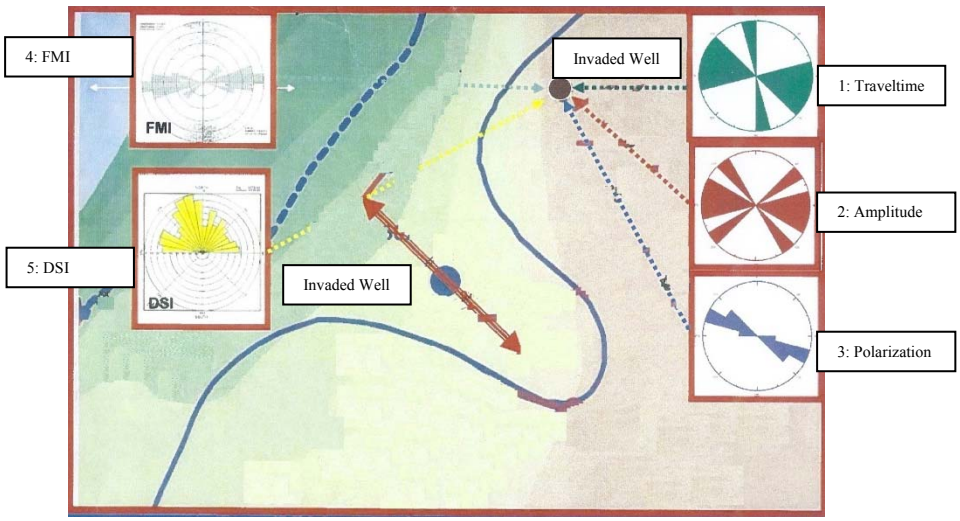

Fig. 24—Water encroachment around the studied area located at the west flank of the field. Water is moving from NW to SE.

Rose Plot 1 is the traveltime, which has a strong correlation with the amplitude fracture direction in Rose Plot 2. This strong correlation may indicate that the same fluid is filling the detected fractures. Owusu et al. (2009) stated that if two sets of fractures are filled with different types of fluid, then the traveltime and amplitude may not be in agreement. The azimuthal variations of the transmitted qP-wave polarization angle of

fracture directions appear in Rose Plot 3. The angle of polarization is the incident angle that was measured from the vertical axis. The need to define formation anisotropy using this angle is discussed earlier (section 4.1.3). The anisotropy directions indicated by the polarization angle rose plot are less scattered than the traveltime and amplitude-fracture directions. Rose Plot 4 and Rose Plot 5 are the fracture orientation from fullbore FMI and DSI, respectively. The anisotropy orientation detected by Rose Plot 4 and Rose Plot 5 is close to the maximum horizontal stress direction.

5.2 Measurements Result from the Invaded Well

5.2.1 VSP Recording Setting in the Uninvaded Well

The VSP survey recorded in the invaded well consisted of 40 shots at an offset of 1090 m and 1098 m from the wellhead and at 9° angular increments. The receiver configuration consisted of a 70-level, 3-C receiver array spaced at 50-ft intervals over the depth range of 3,579 ft to 6,975 ft Water encroachment did not reach the area around the offset well.

The results from VSP of the azimuthal polarization of the compressional-wave anisotropy (**Fig. 25)** show a much stronger polarization in the N-S direction than in the E-W direction.

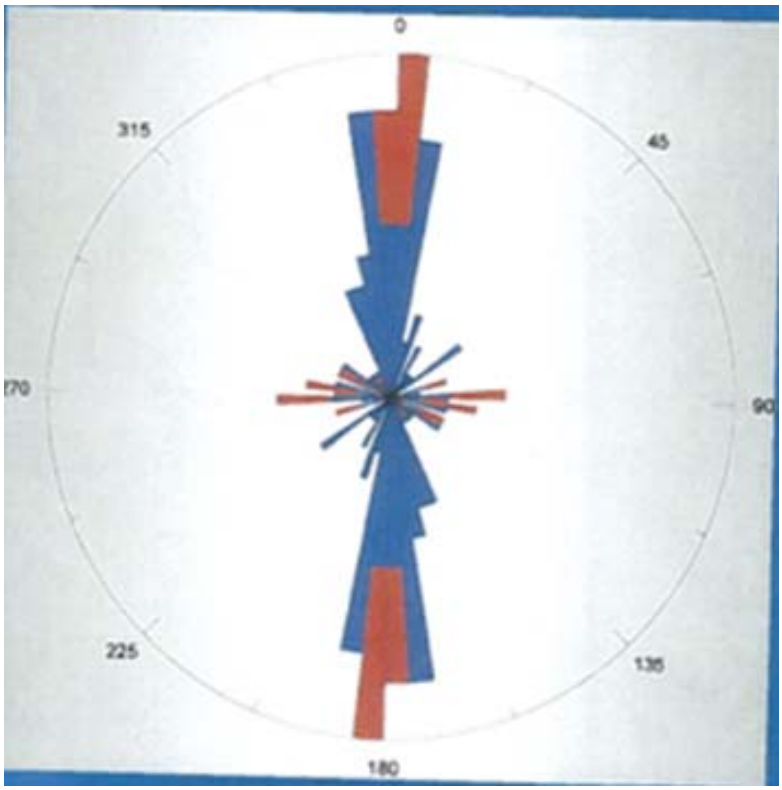

Fig. 25—Result of the azimuthal orientation of P-wave polarization angle anisotropy of the incident angle θ^{o} that is measured from the vertical axis indicates a dominant anisotropy trend in the NS. Some anisotropy is detected in other directions around the EW close to the anisotropy detected by the SWI. The minor anisotropies detected by the VSP could be the same ones detected by the SWI at smaller scale. However, the major anisotropy trends detected by the VSP in the large rock volume overwhelm the smaller anisotropy feature detected by the SWI in the small rock volume.

5.2.2 Openhole Wireline Log Results in the Uninvaded Well

In **Fig. 26** the formation analysis log (FAL) in the first track shows that the formation is mainly limestone with a porosity as good as 20% and decreasing with depth. Also, FAL, in the fifth track, shows that water saturation is 50% in the upper, good-porosity zone

and 100% in the lower zone. The production logging tool (PLT) in the second track shows that the total fluid flow is 100% oil and 0% water. By combining the results from FAL and PLT, we conclude that the water which is seen in FAL is unmovable fluid.

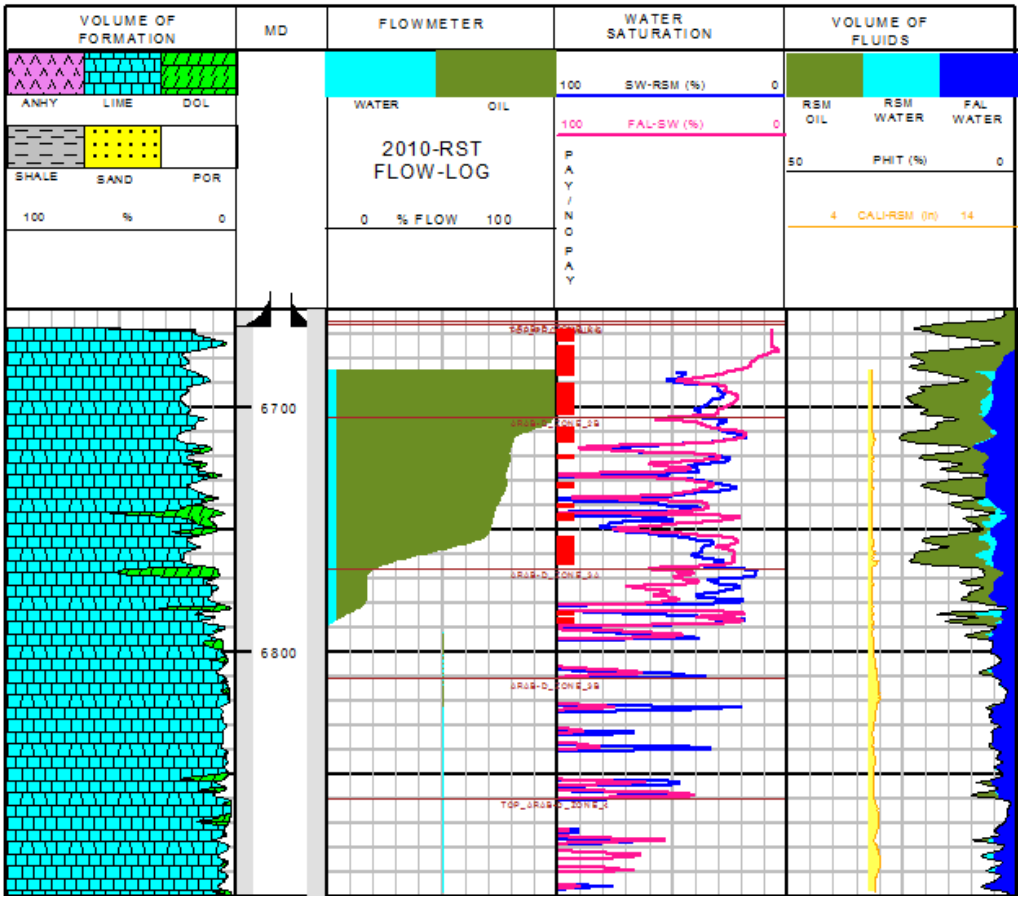

Fig. 26—The result of the formation analysis of openhole logs, production log and the carbon-oxygen log.

The azimuthal shear-wave traveltime anisotropy log and resistivity image **(Fig. 27)** shows the anisotropy in the third track. A high anisotropy is detected between X750 ft

and X870 ft, which also can be seen in the fast azimuth in the fifth track **(Fig. 27)**. The rose plot of the anisotropy in the second track indicates that the anisotropy direction is N-E and more to the east. The resistivity image is helpful in identifying fractures that intersect the borehole wall. In the sixth track, the image log shows some formation lamination, but does not show any major fracture intersecting the borehole.

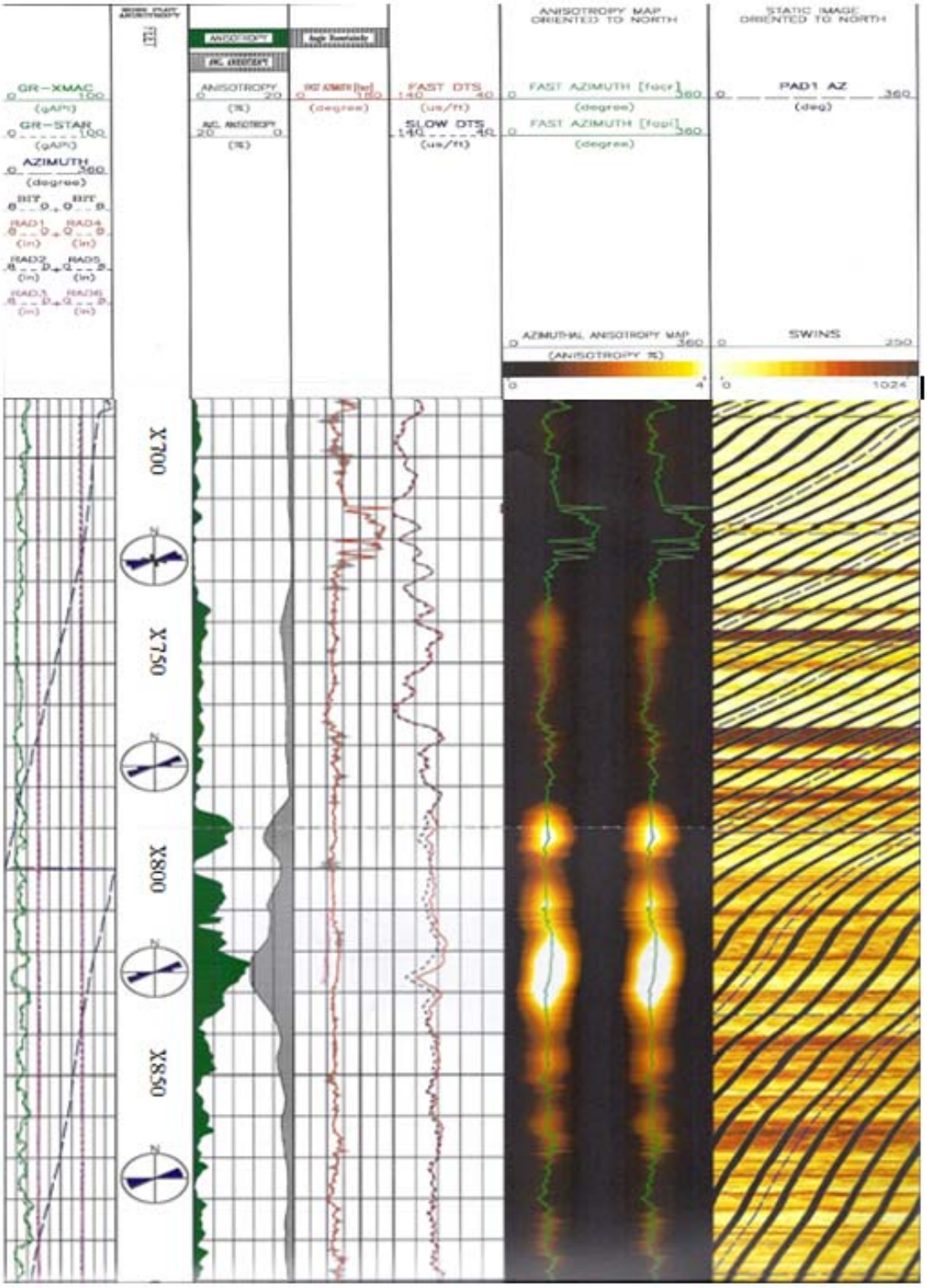

Fig. 27—The result of the azimuthal shear-wave anisotropy indicates a NE-SW anisotropy trend.

CHAPTER VI

DEEP SHEAR IMAGE PROCESS AND ANALYSIS

Single-well acoustic migration imaging was applied to the dipole acoustic waveform data to identify fractures away from the borehole. Prestack frequency-wavenumber FK migration adapted for an acoustic-log configuration was used. Data were processed by modifying parameters until the sonic image was optimized. This report emphasizes methods of finding the right orientation of the fractures by rotating the waveforms to different azimuths around the wellbore. At the first stage, the deep shear wave image was generated with a N-S orientation from one of the two dipoles, which are orthogonal to each other. In **Fig. 28,** gamma ray, caliper, wave slowness, and average slowness are displayed in the first track. Up-reflection and down-reflection are displayed in the third and fifth tracks, respectively. They were generated after separating them from the raw data, which are in the sixth track. The final image result is in the fourth track. To obtain the final image result, the up-reflection and down-reflection were migrated. No fractures have been detected in the N-S direction.

The above process was repeated for the other dipole, which is in the E-W direction (**Fig. 29)**. Again, no fractures were detected. Different parameter values were tried, but the images in the N-S and E-W improved little.

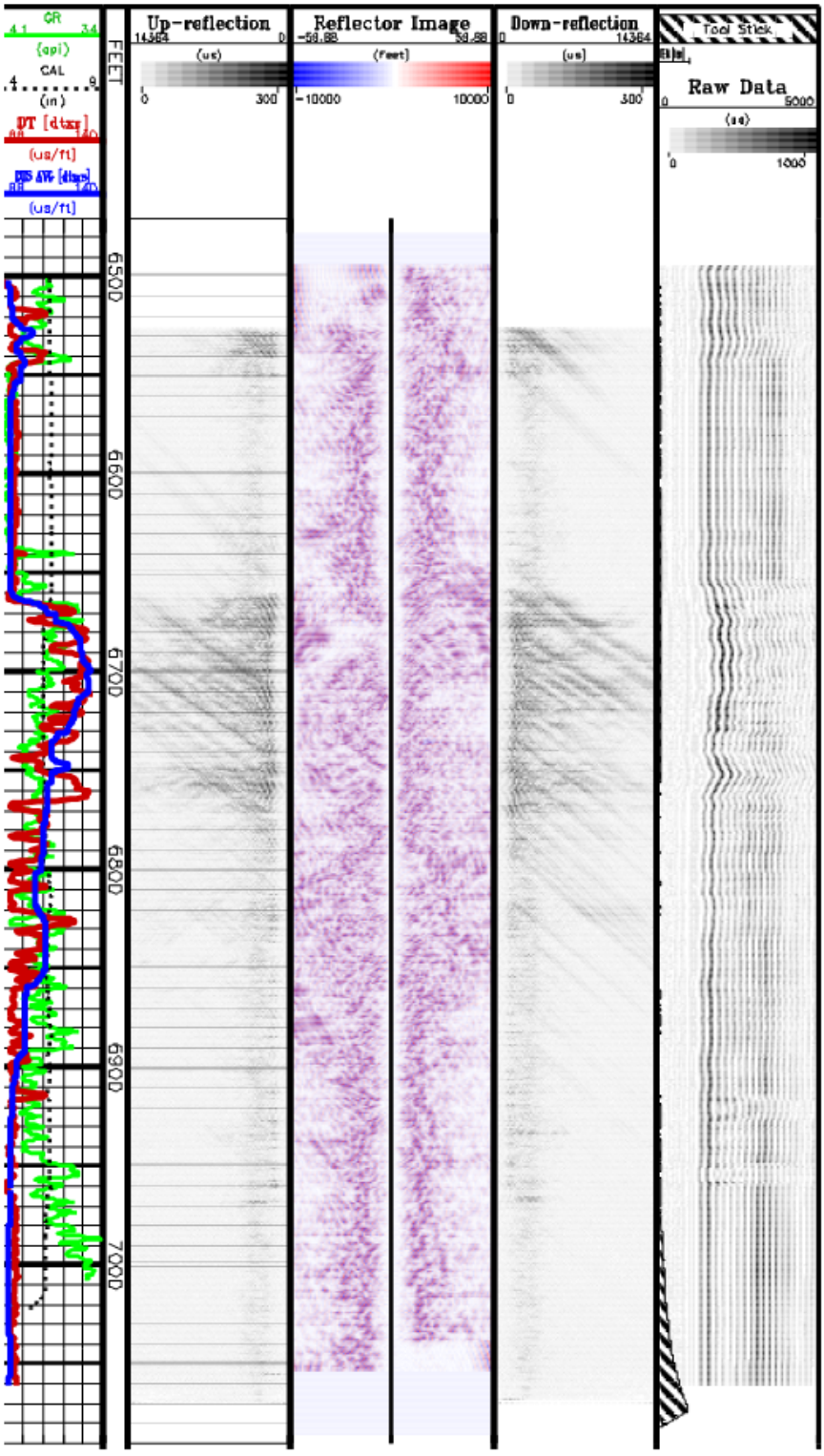

Fig. 28—Deep shear image at N-S. No fractures are apparent this direction.

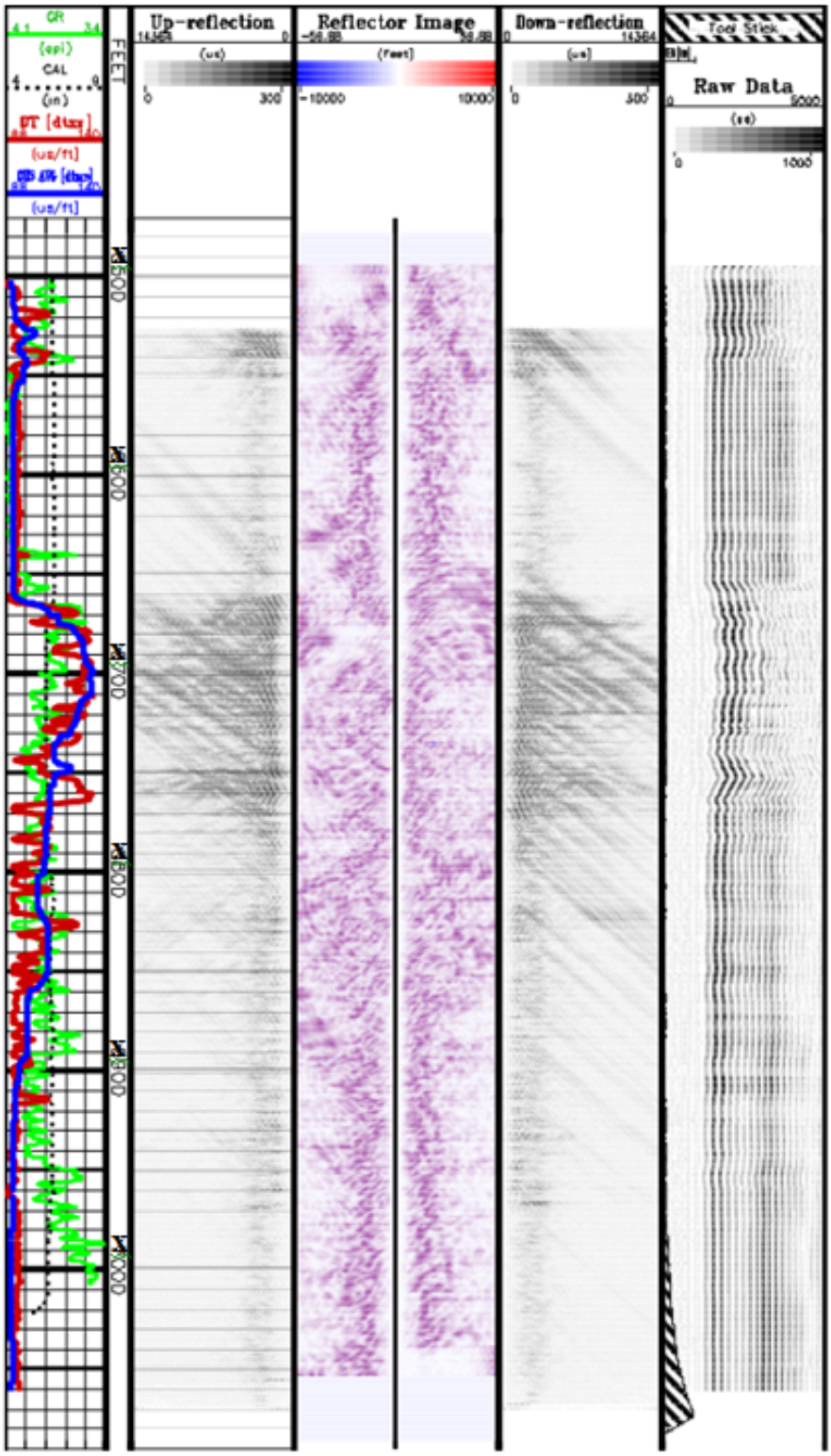

Fig. 29—Deep shear image at E-W. No fractures are apparent this direction.

Since no fracture set or fractures were detected in the original directions, N-S or E-W, I rotated the waveforms around the well. Using Alford rotation, the shear data were projected into the two orthogonal fast and slow shear directions in the presence of shear-wave anisotropy. The next azimuth to test was at 45° (**Fig. 30).** Azimuthal degrees around the borehole start from 0° at the N direction and increase clockwise.

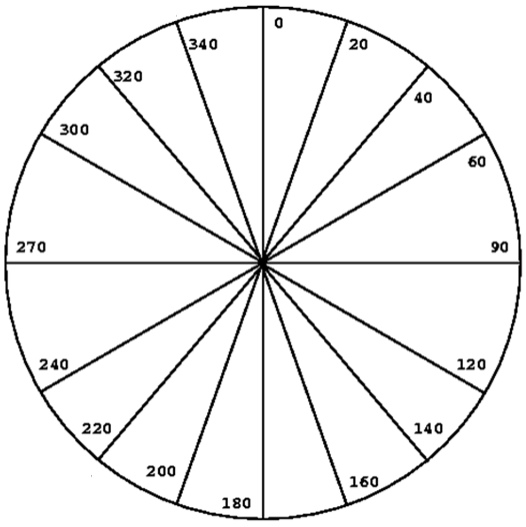

Fig. 30—The various azimuth angles where N is at zero degree.

The image that resulted from rotating the data 45° (**Fig. 31)** shows some features away from the borehole between X750 ft and X850 ft which is the same interval where the high anisotropy had been detected.

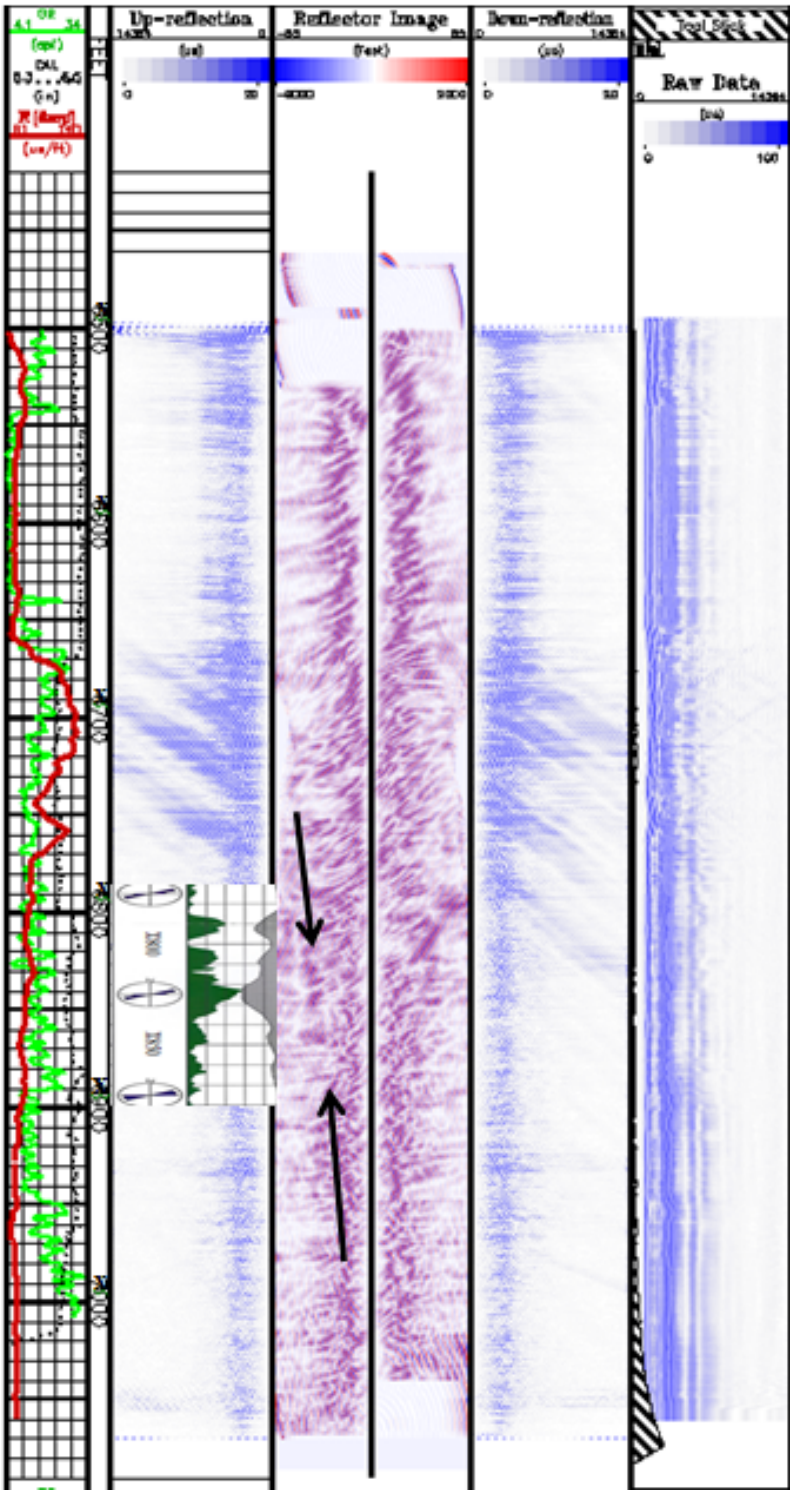

Fig. 31—Deep shear image at 45° N (NE) direction. Anisotropy shows a fracture striking in this direction.

The up-reflection is much stronger and clearer than the down-reflection **(Fig. 30)**. An image also generated for the orthogonal direction at 135° **(Fig. 32)** shows no fractures.

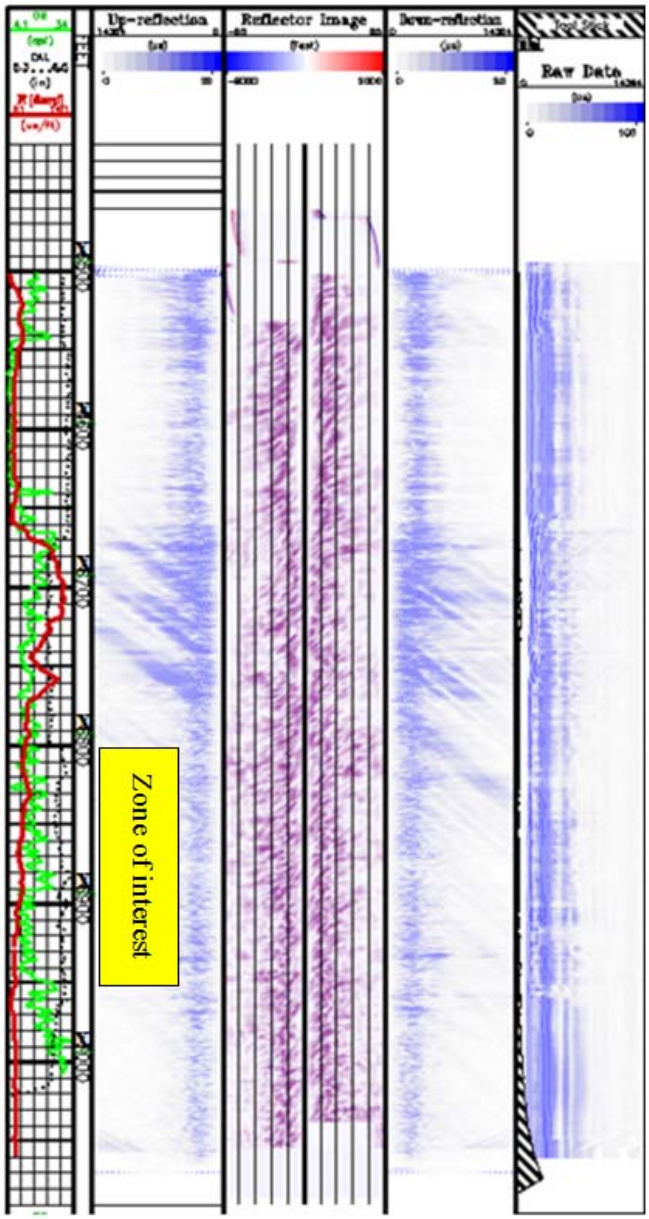

Fig. 32—Deep shear image at SE direction.

For comparison, the N-E and S-E images and the azimuthal anisotropy are displayed in **Fig. 33**; there is a clear fracture between N and E but not between E and S.

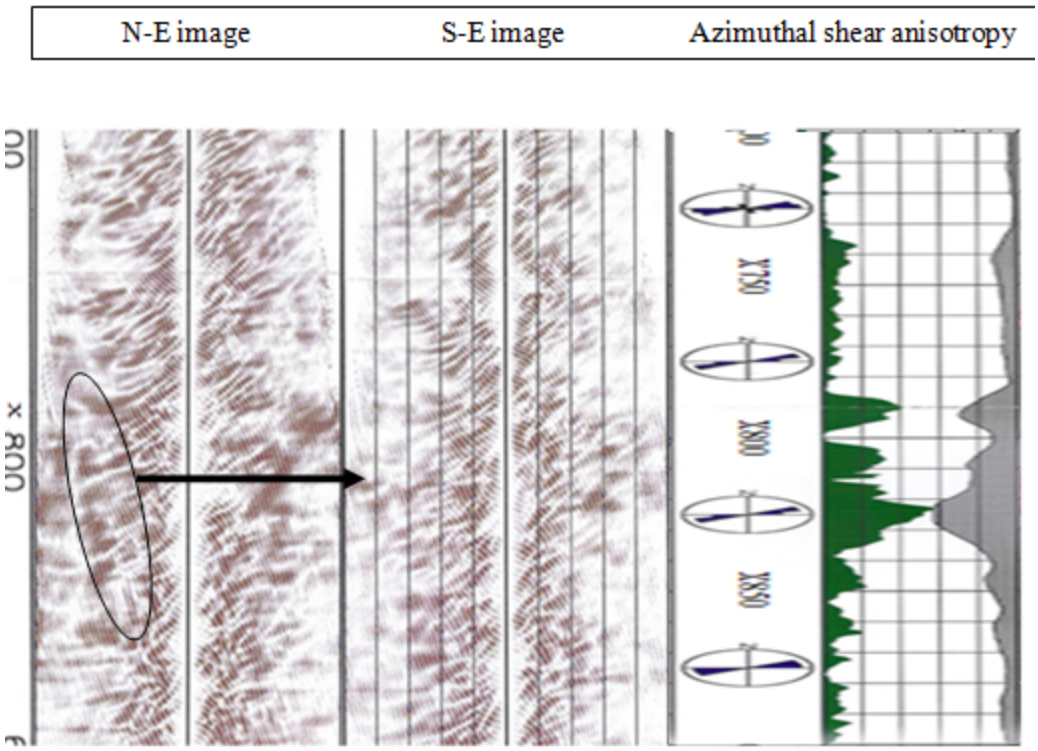

Fig. 33—Deep shear image at 45° from the NS (NE) direction and anisotropy.

To find the actual fracture orientation, the image was rotated in 10° increments around the borehole axis from 0° to 80° (**Fig. 34).**

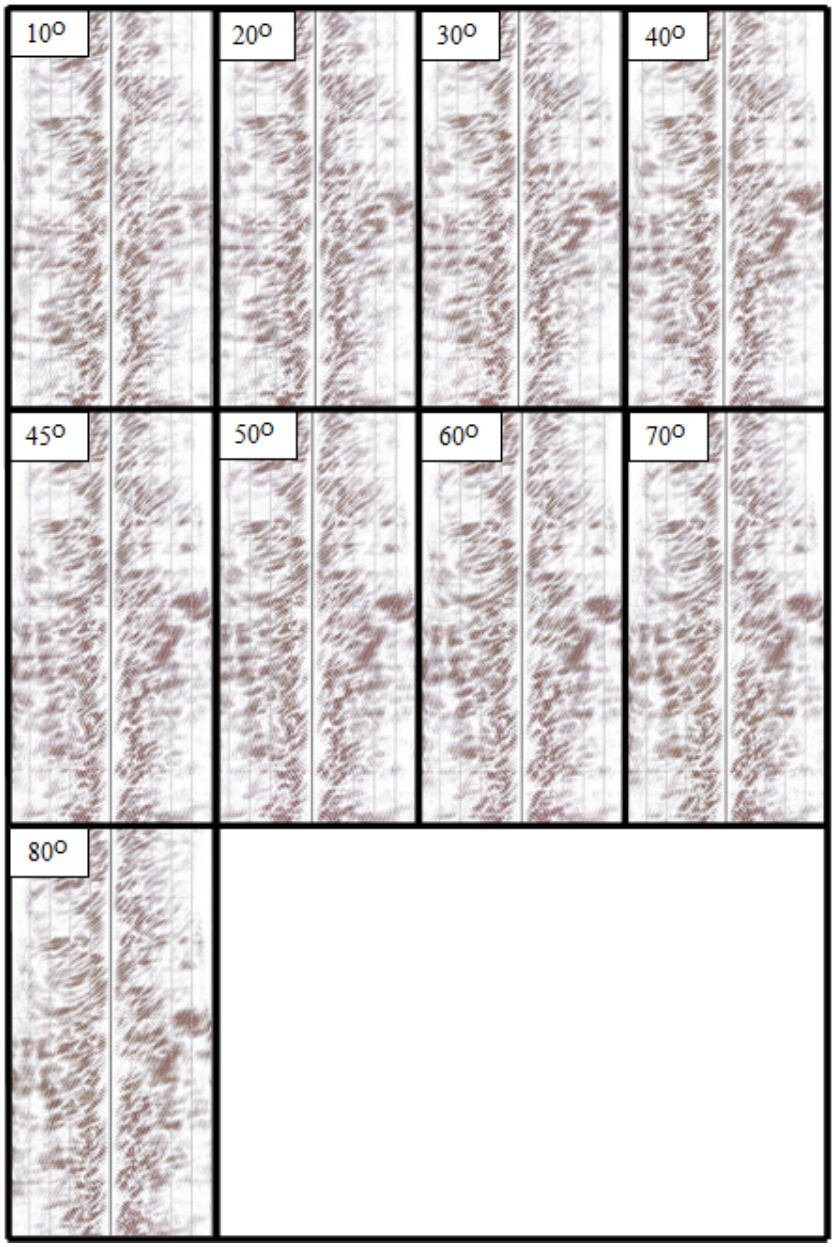

Fig. 34—Comparing images generated at different azimuthal degrees around the borehole axis.

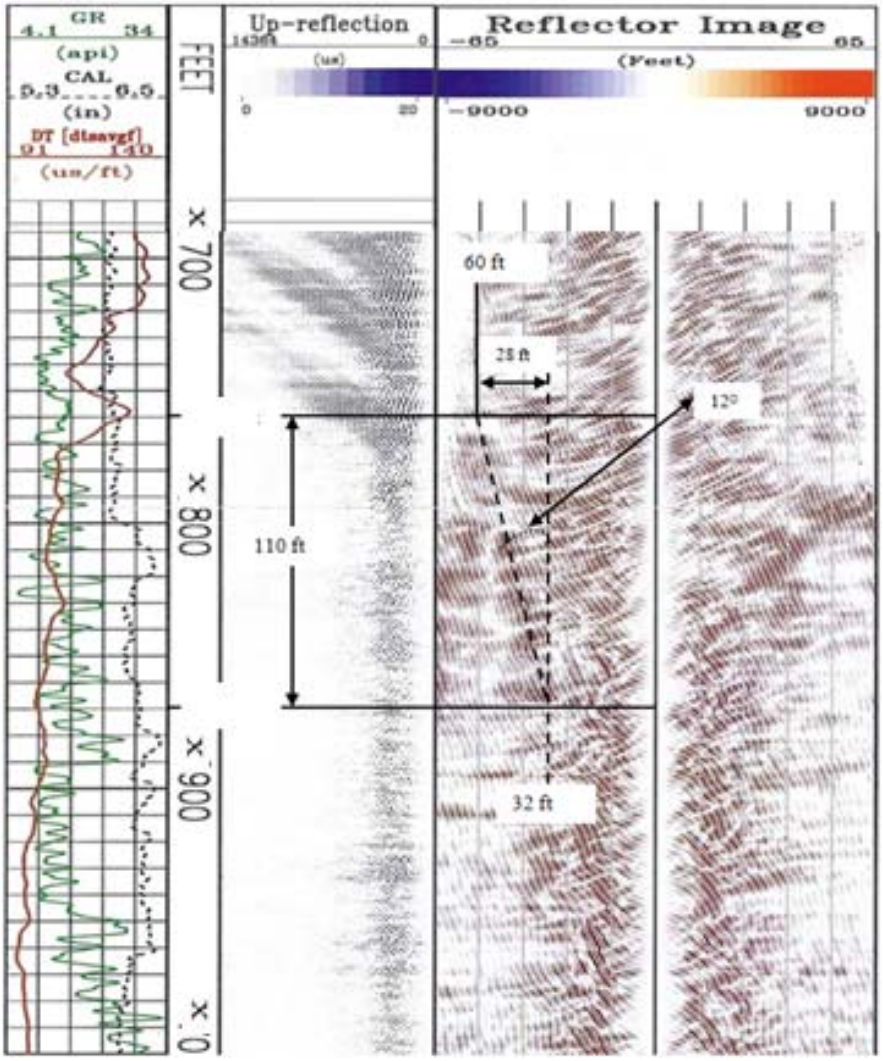

Fig. 35—The detected fracture description.

The image at 60° shows the strongest wave reflection from the fracture of all the images (**Fig. 35**), with clear and continuous indications of the fracture. Parameters were tuned for the image at 60° to enhance the reflection**.** The fracture extends 110 ft from X860 ft to X870 ft. Over this interval, from the top to the bottom, the fracture was clear between

60 and 32 ft away from the borehole wall. The fracture orientation is 60° and its angle of dip is 12° relative to the borehole axis.

Comparing results of the SWI with the production log in the invaded well reveals that the fracture picked by the SWI, at N60E, is in the lower zone, where water is entering the well. The lower zone is not expected to have any fluid flow because of its low porosity and low permeability. Any fluid flow is expected to be in the upper zone, where super-k is identified. However, the fractures in the tight zone at the bottom may flow water to the well.

CHAPTER VII

COMPARE VSP AND DEEP SHEAR IMAGE

While VSP is showing a N-S trend of azimuthal polarization of the compressional-wave anisotropy, single-well acoustic migration imaging shows a fracture more to E-W direction. Several possible factors may cause these results. This study shed the light on many important aspects related to shear image and VSP.

First, the study shows that a process that is affecting the shear image does not necessarily have the same effect on the VSP. The main reason for this is the different scales at which the two tools are operating. While fractures were detectable with shear image, they had no effects on the VSP. The reason is that shear image works in a much smaller frequency range than the VSP. That makes the shear image more sensitive to small features around the well. On the other hand, VSP was successful in detecting the major geological feature at a large scale in the reservoir. Comparing the results from the two methods is not direct, and part of that is that the scaling issue. In the water-invaded well, the large-scale VSP measurement results showed a dominating anisotropy direction to the NS direction while the small scale results from the SWI indicated an N60E anisotropy direction. The VSP measurements picked up what can be called the dominant feature of the reservoir, whereas the SWI detected the smaller, fine details. The VSP looks at the average of a large volume of rock from the production stand point; the VSP must detect the fractures causing the super-k in the upper zone. The cross-dipole

measurement is the smallest scale measurement and has a depth of investigation from 2 to 4 ft. Cross-dipole indicated the same results from the SWI, which detected a fracture 65 ft deep inside the formation. The fracture direction from both cross-dipole and SWI measurements was N60E. This is in the window of the maximum stress direction determined from previous studies (Stenger et al., 2002). From the two different scales of SWI and the cross-dipole, the same trend was observed at the same depth interval between X860 and X870 ft That means the fracture which was detected by the cross-dipole is not only close to the borehole, but extended deep inside the formation.

Second, the results of the VSP derived from the P-wave dipole could be different from shear image results. The main factor is that the P-wave is sensitive to both rock and fluid inside the pores of the rock. However, shear waves do not propagate in fluid and hence they are not affected by the type of fluid inside the rock pores. It is highly recommended that the shear VSP measurements be conducted to compare with both the P-wave VSP and the shear image. If the VSP polarization results estimated from shear wave agree with the shear image, then this will support that the VSP polarization of the P-wave is affected by fluid filling the pores. It is recommended to study fluid effects on VSP measurements derived from P-waves.

Third, in a previous study Owusu et al. (2009) stated that that “the presence of fractures is not the only hypothesis for the water encroachment; the super-k zone (extremely high permeability) zones which occur in numerous wells are also considered a potential

pathway for the water movement." This study shows that there is at least one fracture of 120 ft striking 60° N, and more fractures could be contributing to the water encroachment, but there is no solid evidence to support the hypothesis of the super-k. It would be good to study shear wave images in wells where super-k was noticed. Such a study may results in a correlation between fracture and super-k or redefines super-k as an indication of fractures away from the borehole only detectable by shear images.

CHAPTER VIII

CONCLUSION

Several properties of Haradh field were found from previous studies and from reservoir modeling. These show that maximum horizontal stress in the field ranges between N50E and N90E. Also, it was found that the main three fracture directions are in the N130E, N80E, and N20E directions. For this reason, all the horizontal producer wells were placed in a directional drilling window between N70E to the EW to be parallel to the maximum horizontal stress. This also acts to delay the water breakthrough in the early life of the wells. In contrast, the injector wells were placed perpendicular to the direction of the maximum stress to provide better pressure support.

In a good waterflooding project, water sweep has to be uniform and minimize water production. The presence of fractures generally results in an oriented water production likely to happen in those wells along the preferential flow direction.

Besides the fractures and waterflooding issue, the water contact in Haradh field in the west flank is higher and fresher than the east. These properties were linked to Wadi Sabha, which is a dry riverbed crossing Harahd field from west to east. This water riverbed had to be active in the past and causes the tilting of the oil/water contact now.

Water coning was found in the west flank of Haradh field and many wells experienced water production and waterout in the early stages of their life. The VSP measurements that were recorded in two observation wells in the west flank were not enough to characterize the waterflooding issues. I performed single-well imaging in the water-invaded well to compare it to the results of VSP measurements in the same well and in an offset, uninvaded well.

The heterogeneity of the rock being sampled plays a vital role because if there are two different fracture systems and the SWI evaluated one fracture system at a smaller scale than the VSP, then we could be sampling two different volumes of rock that do not have to be related. It is clear from our previous discussion of the field that the reservoir is very heterogeneous, which makes the scaling problem more difficult, especially with the existence of different fracture systems. An important observation is that the azimuth difference between the major fracture direction N20E and N80E is 60°, which is the same azimuth difference I found between the VSP and the SWI anisotropy directions. Looking carefully into the fracture map, one can trace some curvatures in the fracture systems direction, and at some point this curvature may reach to 90° **(Fig. 7)**. Because of localized variation of the reservoir heterogeneity from one place to another, different results can be found at different places in the reservoir even if the same measurement method was used. That explains the discrepancy between the results of the two VSP measurements made in the two wells. Results from cross-dipole, SWI, and VSP are summarized in **Table 3**.

TABLE 3—MEASUREMENTS SUMMARY

	Cross-dipole	SWI	VSP
Data Provider (Analyzer)	Baker Hughes	Provided by Baker Hughes and processed by the author	Saudi Aramco
Anisotropy Detection	• Depth interval from X860 to X870 ft • Direction is around N60E • 2-4 ft away from the well	• Depth interval from X860 to X870 ft • Direction is around N60E • Up to 65 ft away from the well	• Depth interval from 3,579 to 6,975 ft • Major anisotropy at NS • Smaller anisotropy indications scattered in different directions • > 100 ft away from the well
Possible Interpretation	• A small fracture around borehole • Local stress	• Bed boundary • A Fracture	• Bed boundary • Major fault • Large fracture
Page (s)	48-50	51-60	43-48

Comparing all the measurements are compared together **(Fig. 36)** shows that the water production comes from the lower porosity zone as defined by the porosity and the production logs. Cross-dipole and SWI say this fracture is oriented N60E. The VSP evaluated a larger interval of the well than SWI and cross-dipole. VSP shows a dominating fracture system to the NS direction which could be the super-k zone at the

upper interval of the well. The smaller, scattered anisotropy indications could be small fractures in the low-porosity zone.

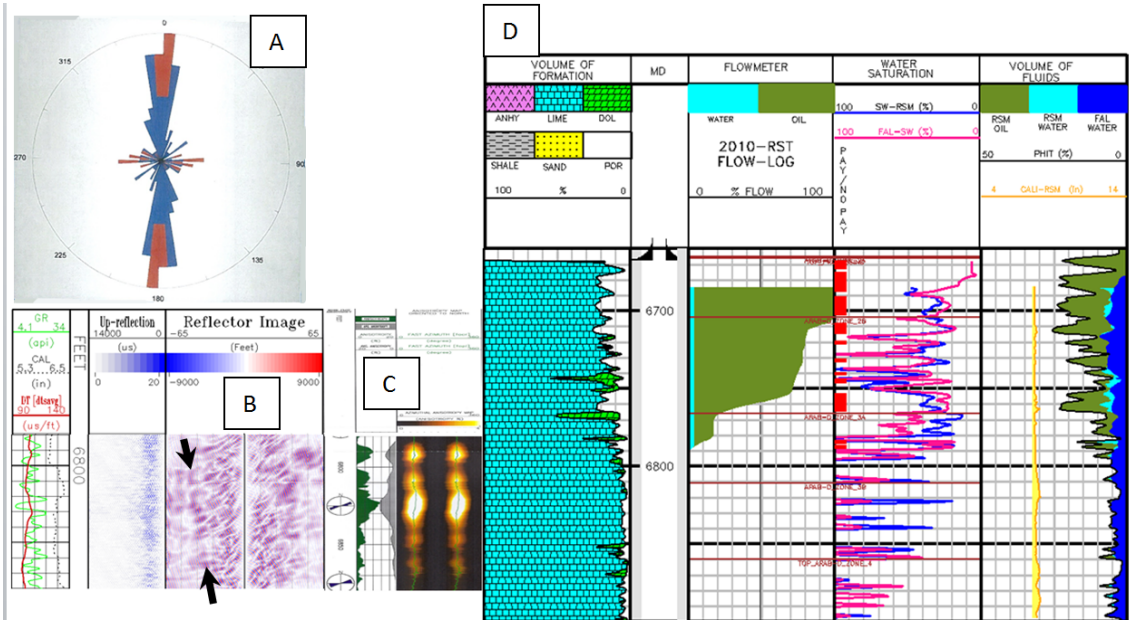

Fig. 36—Comparing all data to each other. (A) Results from VSP data indicating a major anisotropy at the NS orientation. (B) The fracture image that resulted from the SWI data processing marked by arrows. (C) Anisotropy indication observed by the cross-dipole tool. (D) Openhole wireline and production log data show high porosity at the top interval where the high oil production comes from and the low-porosity zone where water enter the well.

8.1 Conclusions

- Based on the given measurements of cross-dipole and SWI, the fractures system align with the maximum horizontal stress direction.
- Fractures which are observed by measurements at 2 to4 ft from the borehole have lateral extent up to 65 ft into the formation, as determined by SWI.

- The fractures are located by cross-dipole and SWI in the tight zone of the reservoir. Water flow into the reservoir from this interval was identified using the production log. That means this fracture system is the source of the water.
- The fracture imaged by SWI extends 110 ft from X860 ft to X870 ft.
- The fracture is clear in the SWI image between 60 and 32 ft away from the borehole wall.
- SWI shows that the fracture orientation is 60° and its angle of dip is 12° relative to the borehole axis.
- The fractures determined by VSP in the NS direction are mostly the fractures responsible for the super-k in the high oil production zone.
- Reservoir modeling does not take into consideration the tight zone of the reservoir, where we believe water production occurs into the well through a previously undetected fracture system.
- Vertical wells should be drilled in the lower zone below Arab D Zone 2B reservoir. Although Arab D Zone 3B looks tight, a fracture system exists and may conduct water to wells drilled through this zone.
- Plugs must be set at the top of Arab D Zone 3 to shut off water in the invaded wells.

Horizontal wells should not be only drilled parallel to the maximum horizontal stress direction, but also have to be drilled as close as possible to the top of Arab D Zone 2A.

REFERENCES

Afifi, A.M. 2005 Ghawar: The Anatomy of the World's Largest Oil Field. http://www.searchanddiscovery.com/documents/2004/afifi01/. Accessed 6 November 2011.

Al-Anazi, B.D. 2007. What You Know About the Ghawar Oil Field, Saudi Arabia? *CSEG* **32** (4): 40-43.

Al-Mubarak, S.M., Pham, T.R., Shamrani, S.S. and Shafiq, M.. 2007. Using Down-Hole Control Valves to Sustain Oil Production from the First Maximum Reservoir Contact, Multilateral and Smart Well in Ghawar Field: Case Study. Paper SPE 11630 presented at the International Petroleum Technology Conference, Dubai, U.A.E., 4-6 December 2007.

Anderson, S. and Nehorai, A. 1996. Analysis of a Polarized Seismic Wave Model *IEEE Transactions on Signal Processing* **44** (2): 379-386.

Bu-Hulaigah, E.H., Stenger, B.A., Pham, T.R. and Van Lingen, P.P. 2001. Developing a Carbonate Reservoir with Fractures and Stratiform High Permeabilities. Paper presented at the OAPEC Conference Paris, France, 28–30 June 2001.

Close, D., Cho, D., Horn, F. and Edmundson, H. 2009. The Sound of Sonic: A Historical Perspective and Introduction to Acoustic Logging. *CSEG Recorder* **34** (5): 34-43.

Crain, E.R. and Eng, P. 2004 How Many Acoustic Waves Can Dance on the Head of a Sonic Log? Canadian well logging society publication, www. spec2000. net/freepubs/AcousticWaves. pdf.

Croft, G. 2011 The Ghawar Oil Field, Saudi Arabia. Greg Croft Inc. http://www.gregcroft.com/ghawar.ivnu. Accessed 27 October 2011.

Dulaijan, K.A., Owusu, J.C., and Weber, D.C. 2011. Azimuthal Anisotropy Analysis of a Walkaround VSP: A Case Study from Saudi Arabia. Paper EAGE BG25 Gpresented at the Borehole Geophysics Workshop - Emphasis on 3D VSP, Istanbul, Turkey, 16 - 20 January 2011.

Fortin, J., Rehbinder, N., and Staron, P. 1991. Reflection Imaging around a Well with the Eva Full-Waveform Tool. *Log Analyst* **32** (3): 271-278.

Haldorsen, J.B.U., Johnson, D.L., Plona, T. Sinha, B.,Valero, H.P. and Winkler, K. 2006. Borehole Acoustic Waves. *Oilfield Rev* **18**: 34–43.

Hardage, B.A. 2000. Vertical Seismic Profiling: Principles: Pergamon Pr., Amsterdam - Lausanne - New York - Oxford - Shannon - Singapore - Tokyo

Hornby, B.E. 1989. Imaging of near Borehole Structure Using Full Waveform Sonic Data. *Geophysics* **54**: 747-757.

Li, Y., Zhou, R., Tang, X. Jackson, J. C. and Patterson, D. J. 2002. Single-Well Imaging with Acoustic Reflection Survey at Mounds. Paper presented at the EAGE 64th Conference & Exhibition, Florence, Italy, 27-30 May 2002.

Owusu, J.C., Mubarak, S.M., and Liu, Q. 2009. High-Fidelity Walkaround VSP Anisotropy Analysis. *The Leading Edge* **28** (8): 966-972.

Paillet, F.L. and Cheng, C.H.A. 1991. *Acoustic Waves in Boreholes*. Boca Raton FL: CRC.

Pham, T.R., Stenger, B.A., Al-Otaibi, U.F., Al-Afaleg N.I., Al-Ali, Z.A. and Sarda S. 2003. A Probability Approach to Development of a Large Carbonate Reservoir with Natural Fractures and Stratiform Super-Permeabilities. Paper SPE 81433 presented at the Middle East Oil Show, Bahrain 9-12 June 2003.

Simmons, M.R. 2005. *Twilight in the Desert: The Coming Saudi Oil Shock and the World Economy*. 1. New Jersey: John Wiley and Sons.

Sorkhabi, R. The King of Giant Fields. GEOExpro http://www.geoexpro.com/magazines/4_10_preview.pdf. Accessed 4 November 2011.

Stenger, B.A., Ameen, M.S., Al-Qahtani, S., Pham, T.R. 2002. Pore Pressure Control of Fracture Reactivation in the Ghawar Field, Saudi Arabia. Paper SPE 77642 presented at the SPE Annual Technical Conference and Exhibition, San Antonio, Texas, 29 September-2 October 2002.

Stenger, B.A., Pham, T.R., Al-Sahhaf, A.A. et al. 2001. Assessing the Oil Water Contact in Haradh Arab-D. Paper SPE 71339 presented at the SPE Annual Technical Conference and Exhibition, New Orleans, Louisiana, 30 September- 3 October 2001.

Tang, X. 2004. Imaging near-Borehole Structure Using Directional Acoustic-Wave Measurement. *Geophysics* **69** (6): 1378-1386.

Tang, X., Zheng, Y., and Patterson, D. 2007. Processing Array Acoustic-Logging Data to Image near-Borehole Geologic Structures. *Geophysics* **72** (2): E87-E97.

Tang, X.M. and Patterson, D.J. 2009. Single-Well S-Wave Imaging Using Multicomponent Dipole Acoustic-Log Data. *Geophysics* **74** (6): WCA211.

Tang, X.M., Zheng, Y., and Patterson, D. 2006. Processing Acoustic Logging Data to Image near-Borehole Geological Structures. *SEG Technical Program Expanded Abstracts* **25** (1): 339-343.

Voelker, J. 2004. A Reservoir Characterization of Arab-D Super-K as a Discrete Fractures Network Flow Systen, Ghawar Field, Saudi Arabia. Ph. D. Dissertation Stanford University, California

Weber, D.C., Dulaijan, K.A., and Owusu, J.C. 2011. Walkaround VSP for Fracture Detection in Northern Saudi Arabia: A Case Study. Paper presented at the Borehole Geophysics Workshop - Emphasis on 3D VSP, Istanbul, Turkey, 16 - 20 January 2011.

Yamamoto, H., Watanabe, S., Koelman et al. 2000. Borehole Acoustic Reflection Survey Experiments in Horizontal Wells for Accurate Well Positioning. Paper SPE 65538 presented at the SPE/CIM International Conference on Horizontal Well Technology, Calgary, Alberta, Canada6-8 November 2000.

VITA

Name: Hussian Abdulhadi A. Aljeshi

Address: Saudi Aramco Oil Company, Dhahran, Saudi Arabia.

Email Address: jeshi79@gmail.com

Education: B.S., Petroleum Engineering, King Fahd University of Petroleum and Minerals, 2002

M.S., Petroleum Engineering, Texas A&M University, 2012